Monthly Notices
of the
ROYAL ASTRONOMICAL SOCIETY

MNRAS **500,** 1–21 (2021)
Advance Access publication 2020 October 22

doi:10.1093/mnras/staa3217

A new era of fine structure constant measurements at high redshift

Dinko Milaković [1]★ Chung-Chi Lee [2] Robert F. Carswell [3] John K. Webb [4] Paolo Molaro [5] and Luca Pasquini [1]

[1]*European Southern Observatory, Karl-Schwarzschild-str 2, D-85748 Garching bei München, Germany*
[2]*DAMTP, Centre for Mathematical Sciences, University of Cambridge, Cambridge CB3 0WA, UK*
[3]*Institute of Astronomy, Madingley Road, Cambridge CB3 0HA, UK*
[4]*School of Physics, University of New South Wales, Sydney, NSW 2052, Australia*
[5]*INAF-Osservatorio Astronomico di Trieste, Via G.B. Tiepolo 11, I-34143 Trieste, Italy*

Accepted 2020 October 12. Received 2020 September 30; in original form 2020 August 24

ABSTRACT

New observations of the quasar HE0515−4414 have been made, aided by the Laser Frequency Comb (LFC), using the HARPS spectrograph on the ESO 3.6m telescope. We present three important advances for α measurements in quasar absorption spectra from these observations. First, the data have been wavelength calibrated using LFC and ThAr methods. The LFC wavelength calibration residuals are six times smaller than when using the standard ThAr calibration. We give a direct comparison between α measurements made using the two methods. Secondly, spectral modelling was performed using Artificial Intelligence (fully automated, all human bias eliminated), including a temperature parameter for each absorption component. Thirdly, in contrast to previous work, additional model parameters were assigned to measure α for each individual absorption component. The increase in statistical uncertainty from the larger number of model parameters is small and the method allows a substantial advantage; outliers that would otherwise contribute a significant systematic, possibly corrupting the entire measurement, are identified and removed, permitting a more robust overall result. The $z_{\rm abs} = 1.15$ absorption system along the HE0515−4414 sightline yields 40 new α measurements. We constrain spatial fluctuations in α to be $\Delta\alpha/\alpha \leq 9 \times 10^{-5}$ on scales $\approx$20 km s^{-1}, corresponding to $\approx$ 25 kpc if the $z_{\rm abs} = 1.15$ system arises in a 1Mpc cluster. Collectively, the 40 measurements yield $\Delta\alpha/\alpha = -0.27 \pm 2.41 \times 10^{-6}$, consistent with no variation.

Key words: techniques: spectroscopic – intergalactic medium – quasars: absorption lines – quasars: individual: HE0515−4414 – dark energy – cosmology: observations.

1 INTRODUCTION

Fundamental constants, such as the fine structure constant ($\alpha \equiv \frac{1}{4\pi\epsilon_0}\frac{e^2}{\hbar c}$) and the proton-to-electron mass ratio ($\mu \equiv \frac{m_p}{m_e}$), are expected to vary in some modifications of General Relativity. A scalar field ϕ coupling to the baryonic matter can produce temporal and/or spatial α variations (Bekenstein 1982; Sandvik, Barrow & Magueijo 2002; Copeland, Nunes & Pospelov 2004; Marra & Rosati 2005; Shaw & Barrow 2005; Barrow & Lip 2012). α may also vary with gravitational potential (Dicke 1959; Sandvik et al. 2002; Mota & Barrow 2004b, a), or via interactions of baryonic matter with dark matter candidates (Olive & Pospelov 2002; Stadnik & Flambaum 2015), or if the vacuum expectation value of ϕ depends on the local density (Silva et al. 2014). In theories with extra spatial dimensions (e.g. Kaluza-Klein and string theories), expansion (or contraction) of higher dimensions can produce observed changes to the coupling constants in our four-dimensional space time. Recent reviews of varying constants are given by Uzan (2011), Martins (2017).

Variations in α and μ have been explored both on Earth through atomic clock measurements (Rosenband et al. 2008), isotope ratio studies (Damour & Dyson 1996), and in space using astronomical observations of white dwarfs (Berengut et al. 2013; Bainbridge et al. 2017), galaxies (Bahcall, Steinhardt & Schlegel 2004), quasars (Webb et al. 1999; Murphy, Webb & Flambaum 2003; Wilczynska et al. 2015; Ubachs 2018), stars around the supermassive black hole in the Galaxy (Hees et al. 2020), and the cosmic microwave background (Avelino et al. 2001; Planck Collaboration 2015). A comprehensive analysis of 317 quasar absorption systems using the *Many Multiplet method* (Dzuba, Flambaum & Webb 1999b; Webb et al. 1999) hinted at a spatial variation of α, modelled as a dipole with amplitude $\Delta\alpha/\alpha = (\alpha_{\rm Q} - \alpha_0)/\alpha_0 = 1.1 \pm 0.2 \times 10^{-6}$, where $\alpha_{\rm Q}$ are quasar absorption measurements and α_0 is the terrestrial value (Webb et al. 2011; King et al. 2012; Wilczynska et al. 2020).

Echelle spectrographs, using slit-based observations and calibrated using ThAr methods, are prone to long-range wavelength distortions (Molaro et al. 2008; Rahmani et al. 2013; Evans et al. 2014). Such distortions, if present and left uncorrected, can significantly contribute to the total $\Delta\alpha/\alpha$ measurement uncertainty (Evans et al. 2014; Kotuš, Murphy & Carswell 2017). Correction techniques include using additional external calibration information from asteroid observations (Molaro et al. 2013; Rahmani et al. 2013), iodine cells (Griest et al. 2010; Whitmore, Murphy & Griest 2010), solar-twin observations (Whitmore & Murphy 2015), or by

★ E-mail: dmilakov@protonmail.com

using additional model parameters (Dumont & Webb 2017). To a reasonable approximation, the best wavelength correction that could be achieved with any of these methods has an accuracy no better than $\lesssim 30\,\mathrm{m\,s^{-1}}$. For comparison, the best laboratory accuracy of UV wavelengths used for $\Delta\alpha/\alpha$ measurements is $0.01\,\mathrm{m\,s^{-1}}$, three orders of magnitude better. Laser Frequency Comb (LFC; Udem, Holzwarth & Hänsch 2002; Hänsch 2006; Steinmetz et al. 2008) wavelength calibration methods provide a vastly superior calibration than the correction methods above as they provide $3\,\mathrm{m\,s^{-1}}$ accuracy for individual line centre measurements (Milaković et al. 2020; Probst et al. 2020).

In this paper, we report a set of high redshift α measurements from new observations of the quasar HE0515−4414. The observations (described in Section 2) are of very high quality. These data are the first quasar spectral observations where the wavelength calibration has been carried out using an LFC. This means that any wavelength scale distortions present will be negligible. A second spectrum was produced from the same quasar observations but calibrated using ThAr methods. The two spectra enable a unique set of comparative tests to quantify uncertainties in searches for fundamental constant variations.

We use new automated analysis methods (Lee et al. 2020) to produce models for each spectrum and measure α using the Many Multiplet method (Section 3). We introduce a new method, measuring α for each absorption component (rather than an average across an entire absorption complex). This provides considerably more detail and also offers a substantial advantage by enabling systematics to be more readily identified. We summarize our main findings in Section 4 and discuss them in Section 5.

2 DATA

2.1 Data acquisition

The spectrum used in this work was produced from high-resolution ($R = \lambda/\Delta\lambda = 115\,000$) observations using the High Accuracy Radial velocity Planet Searcher (HARPS) echelle spectrograph (Mayor et al. 2003). HARPS is a double-channel echelle spectrograph built for extremely precise spectroscopic measurements. We observed HE0515−0414 (abbreviated as HE0515) between 2018 December 3 and 11 using HARPS in the classical fibre spectroscopy mode, where channel A recorded the HE0515 spectrum and channel B recorded the sky spectrum. We obtained 36 exposures totalling 52h 31m (Table 1). Each exposure was bracketed by ThAr and LFC exposures for wavelength calibration. The sky was dark and the seeing conditions varied between 0.45 and 1.98 arcsec throughout the observing run. The median seeing (i.e. the median of column 3 in Table 1) is 1.34 arcsec. This has no influence on the final spectral resolution. The secondary guiding system ensures the object is consistently centred on the object image up to 0.01 arcsec and octagonal fibres ensure that the light evenly illuminates the spectrograph pupil. Therefore, telescope guiding and fibre illumination are not expected to introduce spectroscopic velocity shifts larger than $0.12\,\mathrm{m\,s^{-1}}$ (Lo Curto et al. 2015).

Light entering the spectrograph is recorded on the detector (a mosaic of two EEV2k4 CCDs) for which the read-out mechanism is located on one of its sides (Mayor et al. 2003; Rodler & Lo Curto 2019). By design, charge transfer occurs in the cross-dispersion direction to minimize effects of charge transfer inefficiency (CTI). Left uncorrected, CTI can introduce spurious spectroscopic velocity shifts up to $3\,\mathrm{m\,s^{-1}}$ for very low flux exposures (Milaković et al. 2020). However, as no appropriate CTI model yet exists for HARPS, we do not correct for this effect.

Table 1. The final co-added spectrum of HE0515−4414 is formed from co-adding 36 HARPS exposures taken in classic spectroscopy mode, totalling 52h 31m. Columns 1 and 2 give the observing time start (in UTC) and the exposure time, respectively. Column 3 gives the average of the telescope seeing recorded at the beginning and the end of observation. Column 4 gives the S/N per extracted pixel at the centre of order 111 (≈ 5500 Å). All quantities are determined from values recorded in headers of `e2ds` HARPS pipeline products.

Observing time (UTC)	Exp. time (s)	Seeing (arcsec)	S/N (pixel^{-1})
2018-12-04T00:27:52.031	5400	1.48	6.4
2018-12-04T02:12:04.582	5400	1.35	11.0
2018-12-04T03:50:40.736	5400	1.54	8.3
2018-12-04T05:36:27.032	5400	1.71	5.6
2018-12-04T07:14:20.953	2700	1.25	3.2
2018-12-05T03:14:39.850	5400	1.91	7.3
2018-12-05T04:52:04.530	5400	0.45	7.1
2018-12-05T06:42:00.250	5400	N/A	7.5
2018-12-06T00:41:08.634	5400	1.98	5.8
2018-12-06T02:30:00.882	5400	1.64	9.0
2018-12-06T04:08:04.226	5400	1.40	4.6
2018-12-06T05:46:25.189	5400	1.58	8.2
2018-12-06T07:25:04.433	5098	1.59	6.4
2018-12-07T00:23:24.209	5400	1.50	7.1
2018-12-07T02:01:11.070	5400	1.33	9.1
2018-12-07T03:38:28.641	4905	1.66	7.2
2018-12-07T05:32:14.425	5400	1.31	7.9
2018-12-07T07:09:39.678	5400	1.40	5.3
2018-12-08T00:32:12.597	4214	1.32	5.0
2018-12-08T02:15:25.854	5400	1.44	5.9
2018-12-08T03:54:16.167	5400	1.32	9.0
2018-12-08T05:32:25.299	5400	1.39	11.4
2018-12-08T07:10:06.569	5400	1.26	9.6
2018-12-09T00:37:46.416	5400	1.29	8.2
2018-12-09T02:22:05.279	5400	1.21	10.1
2018-12-09T03:59:32.258	5400	1.17	9.3
2018-12-09T05:36:04.415	5400	1.10	11.0
2018-12-10T00:24:18.778	5400	1.30	9.2
2018-12-10T02:15:06.228	5400	1.69	9.1
2018-12-10T03:54:46.885	5400	1.23	8.6
2018-12-10T05:32:28.955	5400	1.07	10.6
2018-12-10T07:10:20.256	5400	0.80	13.2
2018-12-11T00:28:14.801	5400	1.04	8.9
2018-12-11T02:12:13.372	5400	1.56	11.2
2018-12-11T03:50:37.414	5400	1.27	10.7
2018-12-11T07:31:21.735	4795	1.05	8.6

Raw images were reduced using the HARPS pipeline (version 3.8; Rodler & Lo Curto 2019). The pipeline extracts 1D spectra of individual echelle orders following optimal extraction by Horne (1986), Robertson (1986). Order tracing and pixel weights are determined from tungsten-lamp frames taken at the beginning of each night. Pipeline products previously demonstrated a $0.01\,\mathrm{m\,s^{-1}}$ precision (Milaković et al. 2020), so we do not expect spectroscopic velocity shifts associated with its use.

2.2 Wavelength calibration and data addition

Wavelength calibration was obtained from LFC and ThAr frames taken immediately before each quasar exposure. The LFC has an offset frequency of 4.58 GHz and 18 GHz line separation. LFC wavelength calibration was performed using eight seventh-order

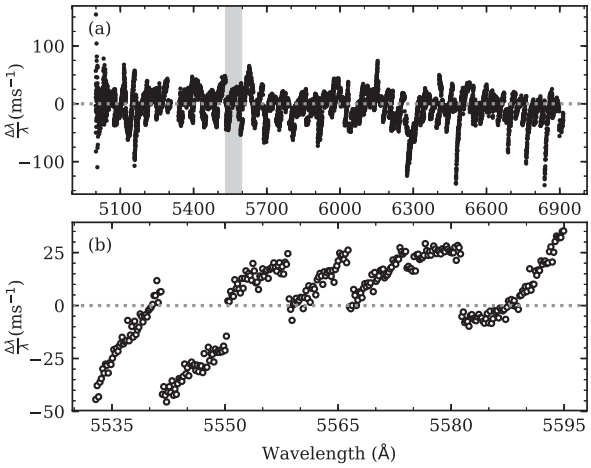

Figure 1. Distortions in the ThAr calibration revealed by comparing with LFC lines. Each dot is a single LFC line. Distortion amplitude generally increases at order edges. Clear discontinuities associated with the HARPS detector stitching pattern (Wilken et al. 2010; Molaro et al. 2013) are seen for all orders. The distortions do not show long-range wavelength dependency, have a $-1.1\,\mathrm{m\,s^{-1}}$ mean offset with respect to the LFC scale, and an overall scatter of $27.9\,\mathrm{m\,s^{-1}}$ rms. Panel (b) shows the region covered by echelle order 110 ($\lambda \approx 5500$ Å), also marked by a grey rectangle in panel (a).

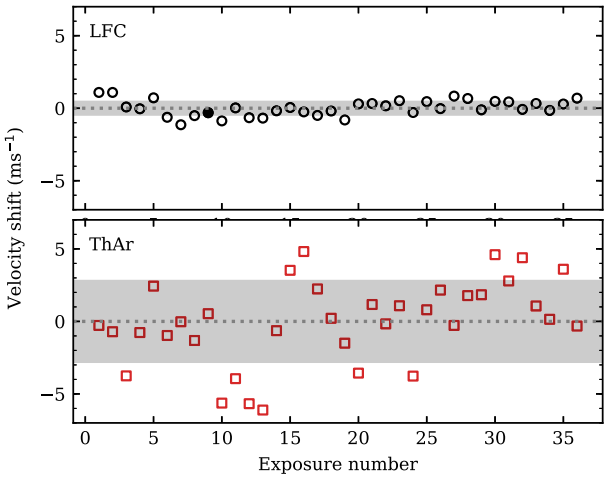

Figure 2. LFC calibration was found to drift by $0.52\,\mathrm{m\,s^{-1}}$ rms over the 8 nights of our run (grey shaded region in the top panel), as measured by shifts of LFC lines on the detector. Over the same period, ThAr calibration experienced drifts of $2.87\,\mathrm{m\,s^{-1}}$ rms (grey shaded region in the bottom panel). Shifts in individual LFC (ThAr) exposures are shown as unfilled black circles (red squares) in the top (bottom) panel. The zero line represents the mean value of all points. Shifts were calculated using echelle orders 88–121 only (those orders best covered by LFC). The filled black circle in the top panel represents the LFC exposure used for wavelength calibration of all quasar exposures (see the text).

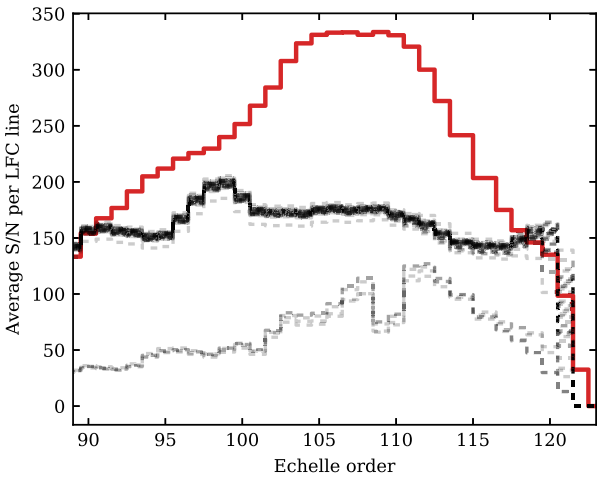

Figure 3. Each histogram shows the average S/N per LFC line in a single LFC exposure as a function of echelle order. Five exposures have significantly lower S/N than others (the reason is unknown). A single exposure (full red histogram) reaches S/N of ≈330 per LFC line and covers one additional echelle order (122). This exposure provides the most accurate wavelength calibration over the broadest wavelength range. Given the exquisite stability of HARPS (see Fig. 2), we choose to use this exposure to calibrate all quasar exposures.

polynomials per echelle order. Each echelle order spans eight 512-pixel blocks on the CCD (Wilken et al. 2010; Molaro et al. 2013). The accuracy of the LFC wavelength calibration is $3\,\mathrm{m\,s^{-1}}$, measured by the root mean square (rms) of calibration residuals (i.e. known LFC line frequency minus the frequency determined from the wavelength solution at line position on the detector, see Milaković et al. 2020). The ThAr wavelength calibration was produced by the HARPS pipeline using a single third-order polynomial per echelle order, with an accuracy of $27\,\mathrm{m\,s^{-1}}$. The average difference in the two calibrations, considering wavelengths $\lambda \geqslant 5000$ Å, is $-1.13\,\mathrm{m\,s^{-1}}$ (LFC minus ThAr).

Comparing the true LFC line wavelengths to the ThAr-calibrated wavelengths at their location on the detector reveals a distortion pattern in the ThAr calibration, illustrated on Fig. 1. The pattern shows no long-range wavelength trends, but contains discontinuities associated with stitching of the HARPS detector (Wilken et al. 2010; Molaro et al. 2013), not accounted for by the pipeline calibration procedure. We discuss the impact of this distortion pattern on α measurements in Section 5.

Over the eight nights of our run, the spectrograph stability is $0.52\,\mathrm{m\,s^{-1}}$, as illustrated in Fig. 2.[1] This number was obtained by measuring the average shifts of LFC line positions in individual exposures with respect to their position in the first exposure and calculating the rms. Applying the same method to the ThAr lines gives an rms of $2.87\,\mathrm{m\,s^{-1}}$, six times larger.

Although all LFC exposures were taken under the same nominal conditions and with same exposure times, it turned out that one exposure was substantially better (in terms of flux) than all others (Fig. 3). Therefore, after careful consistency checking between multiple LFC exposures, this highest flux LFC exposure was used to wavelength calibrate all quasar exposures for wavelengths $\lambda \geqslant 5000$ Å (the LFC data cuts off below this wavelength). There are no saturated LFC lines. We do not follow the same procedure for ThAr calibration, but calibrate each quasar exposure using the ThAr frame taken immediately beforehand.

We transform the LFC and the ThAr wavelength scales to the Solar system barycentre rest frame using the barycentric velocity shift correction provided by the HARPS pipeline, independently for each quasar exposure. The barycentric correction provided by the

[1]This is not the same as the precision which can be achieved in the simultaneous referencing observing mode.

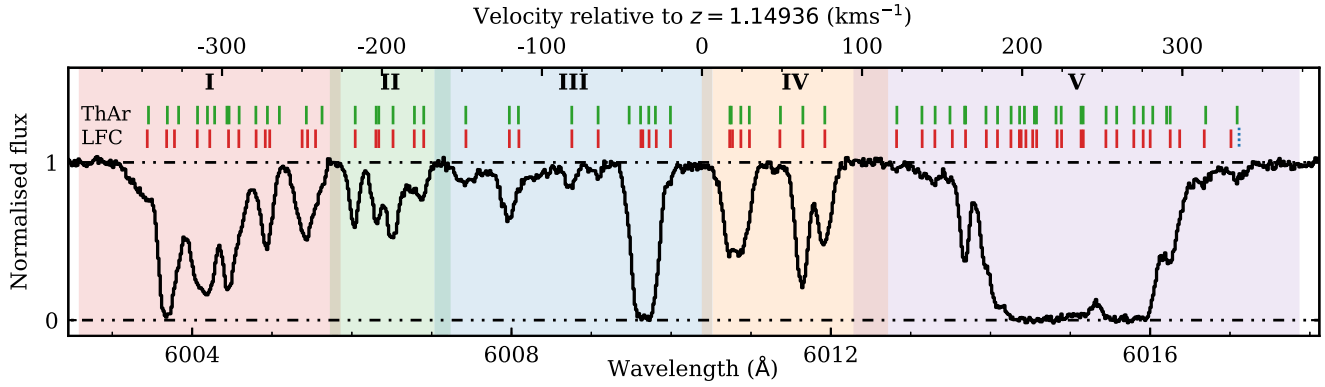

Figure 4. The LFC-calibrated spectrum of HE0515−4414 showing the Mg II λ2796 transition at $z \approx 1.15$ (black histogram). Five coloured areas mark individual regions (denoted by I–V) for which we produce `AI-VPFIT` models and measure $\Delta\alpha/\alpha$. Small overlaps between neighbouring regions enable better continuum level estimation in each region. The solid red (green) ticks above the data indicate individual metal absorption lines in the best-fitting LFC (ThAr) model. The top x-axis shows the velocity with respect to the average redshift of all metal lines in the LFC model, $z = 1.14936$. The blue dashed line at $v \approx 330\,\mathrm{km\,s^{-1}}$ marks the location of an unidentified absorption line in the LFC model. More detailed plots, showing the data, the model, and the residuals can be found in Appendix B (LFC) and Appendix C (ThAr), split by region and transition.

pipeline is based on Bretagnon & Francou (1988) and uses the flux-weighted average time of observation. This value agrees down to several $\mathrm{mm\,s^{-1}}$ with our independent calculation, using the same information and the `astropy` module.[2]

Finally, we rebin the individual extracted spectra on to a common wavelength grid using a custom routine and sum them together, weighting each pixel by its error estimate (which includes the Poissonian error term, the read-out noise, and the dark current). The error array extracted during this procedure agrees with the estimate derived from flux rms over ≈ 1 Å range. The final co-added spectrum has an average signal-to-noise ratio (S/N) near 50 per 0.015 Å pixel in the continuum. This data extraction process was performed for the LFC and ThAr calibration separately, producing two spectra from the same observations.

3 MODELLING PROCEDURE

The spectrum shows a damped Lyman-α absorption complex spanning $700\,\mathrm{km\,s^{-1}}$, at redshift $z_{\mathrm{abs}} \approx 1.15$ (Reimers et al. 1998), from which numerous previous measurements of α have been made (Quast, Reimers & Levshakov 2004; Levshakov et al. 2005, 2006; Chand et al. 2006; Molaro et al. 2008; Kotuš et al. 2017). There are at least 26 transitions useful for an α measurement in this system. The *Many Multiplet* analysis in this work makes use of transitions covered by the LFC calibration, listed in Table A1. None of the transitions we use blend with any other systems nor with transitions from the $z = 0.28$ absorption complex identified by Bielby et al. (2017). The LFC-calibrated spectrum showing the Mg II λ2796 transition is plotted as a black histogram in Fig. 4.

We use the most recent set of laboratory wavelength measurements, transition probabilities, oscillator strengths, and isotopic structures for the relevant transitions. These are given in Table A1. The isotopic abundances were assumed to be solar (Asplund et al. 2009). The sensitivity coefficients that relate atomic line shifts to a change in α are from Dzuba, Flambaum & Webb (1999a), Dzuba et al. (2002), Dzuba & Flambaum (2009). All atomic data is provided as online supplementary material.

We use a fully automated modelling procedure, `AI-VPFIT`, to produce a model of the absorption system (Lee et al. 2020). `AI-VPFIT` is a development of the approach introduced in Bainbridge & Webb (2017) and Bainbridge et al. (2017). Model complexity is increased by placing absorption components ('trial lines') at a random location in the velocity structure and checking if the newly introduced parameters are justified by the data. For the analysis described in the present paper, the optimal number of model parameters are derived using the corrected Akaike Information Criterion (Akaike 1974; Sugiura 1978). Performance tests using simulated data are described in Lee et al. (2020). Redshifts and b-parameters of components appearing in multiple species are tied during fitting (Section 3.2). Column densities are free parameters. We include additional parameters for the unabsorbed continuum level for all transitions and for zero-level adjustment for saturated ones. α is also kept as a free parameter but this has been treated in two different ways (see Sections 3.3 and 3.4). The basis of the AI algorithm is a genetic process in which a model is built up in 6 well-defined stages. An initial model for the absorption system is generated using a 'primary' species, that is, one atomic transition (or atomic species), selected to maximize line strength but avoiding line saturation. Subsequent stages incorporate further atomic species, with appropriately tied parameters, refine parameter errors, check for overfitting, and allow for 'interlopers', i.e. unidentified lines from other redshift systems that are needed to derive a statistically acceptable overall model.

We produce models for the LFC-calibrated and ThAr-calibrated spectrum independently. All relevant settings during `AI-VPFIT` modelling are kept the same (such as the number of attempts `AI-VPFIT` will make to increase model complexity before proceeding to the following stage, default parameter values for trial lines, line dropping criteria, finite derivative step sizes, etc.), ensuring that all the differences between the final models are a direct consequence of differences in the input data. We refer to models produced from the LFC- and the ThAr-calibrated spectrum as the LFC and the ThAr models, respectively. Figures showing the data, the models, and the residuals for all transitions and all regions are in Appendices B (for LFC) and C (for ThAr).

[2] https://docs.astropy.org/en/stable/coordinates/velocities.html

3.1 Instrumental profile

The nominal HARPS instrumental profile has a full width at half-maximum of 2.61 km s^{-1}. The average *b*-parameter for individual absorption components in the absorption system analysed in this paper is ≈5 km s^{-1}. The observed quasar lines are thus well-resolved. When matching models to the observed data we must convolve Voigt profiles with the HARPS instrumental profile (IP). To do this we used a Gaussian IP. However, slight departures from a Gaussian have been reported. Moreover, these are found to vary with both flux and position on the detector Milaković et al. (2020). A numerical profile determined directly from HARPS calibration data would thus provide a slightly more accurate IP. However, this was not possible due to insufficient available data.[3]

3.2 Temperature as a free parameter

The choice of a line broadening mechanism heavily influences the final model. We found that using turbulent broadening (i.e. not including temperature as a free parameter) impacts significantly on the analysis. For example, imposing a turbulent model forces *b* to be the same for all species irrespective of atomic mass. If turbulent broadening does not apply in practice, the consequence of the assumption is that additional velocity components are unavoidably included in order to achieve a satisfactory fit to the data. The converse is true - i.e. if a pure thermal model is imposed in the modelling procedure, additional velocity components may also be required to compensate if the model is inappropriate. We explored this by computing models for all three cases, i.e. turbulent, thermal, and mixed-*b*.

In the mixed-*b* model, the total line *b*-parameter is

$$b^2 = b_{\rm turb}^2 + \frac{2kT}{m}, \quad (1)$$

where the right-hand-side terms are the turbulent and thermal contributions, respectively. In the thermal contribution, k is the Boltzmann's constant, T is gas temperature, and m is the appropriate atomic mass. The contribution of each broadening mechanism is determined by the relative widths of transitions of different atomic masses.

The interesting outcome was that a mixed-*b* model generally requires fewer components and also avoids spurious double-components in line centres (see Lee et al. 2020). Further, once mixed-*b* models have been derived, it becomes apparent that temperature parameters are genuinely required by the data. The weighted average temperature is $T = 9.12 \pm 1.08 \times 10^3$ K. Individual temperature measurements are shown in Fig. 5. The temperature is poorly estimated for some components (due to line blending and/or weak lines). Similar results are obtained for the ThAr-calibrated spectrum (not reported). The normalized χ^2 of temperature measurements from 62 velocity components is 1.042, so the data appear to be consistent with a single temperature applying to all components.

[3]The IP is known to be flux-dependent. We do not have a suitable set of LFC exposures to determine the IP as a function of flux level. Data from Probst et al. (2020) and Milaković et al. (2020) are not useful for this purpose because the HARPS fibres were exchanged since that data were taken, thus changing the IP (Lo Curto et al. 2015).

3.3 Subdividing the absorption complex – 5 regions

We initially divide the system into five regions, I–V (coloured regions in Fig. 4). Partitioning occurs where the normalized continuum recovers to unity. There is slight overlap between continuum regions in order to optimize continuum estimates. This partitioning has the benefit of simplifying computations and providing independent α measurements, whilst avoiding any potential bias that could occur if unidentified line blending corrupts part of the data.

The five $\Delta\alpha/\alpha$ measurements derived from splitting the absorption system into regions are tabulated in Table 2. The quoted uncertainties are derived from the covariance matrix at the best solution. Other relevant statistical information, i.e. the number of free parameters for each region, the number of metal components and their average redshift, and the reduced χ^2 of the model ($\chi^2_\nu = \chi^2/\nu$, where ν is the number of degree of freedom in the model), are also given. The weighted average of $\Delta\alpha/\alpha$ measurements over all five regions for the LFC-calibrated spectrum is $0.94 \pm 1.97 \times 10^{-6}$. The same quantity for the ThAr-calibrated spectrum is $4.82 \pm 1.92 \times 10^{-6}$.

For the LFC-calibrated spectrum, the α measurements from regions I, III, IV, and V are consistent with no variation in α. However, region II produces the seemingly anomalous result of $\Delta\alpha/\alpha = 17.74 \pm 4.30 \times 10^{-6}$ (i.e. a 4.1σ deviation from zero). For the ThAr-calibrated spectrum, regions III, IV, and V are all consistent with $\Delta\alpha/\alpha = 0$. However, regions I and II are not. Region II produces a non-zero result that is similar to the LFC spectrum. Region I also gives a strongly positive result. We discuss ways in which such anomalies can arise in Section 3.4.

3.4 Further subdivision – 47 measurements of α

Instead of dividing the complete absorption complex into five segments and obtaining five measurements of $\Delta\alpha/\alpha$, we can instead solve for the best-fitting model using one free $\Delta\alpha/\alpha$ parameter for each individual absorption component in the complex. Doing so provides considerably more detail and can identify any $\Delta\alpha/\alpha$ outliers that might 'corrupt' an α measurement derived over a whole region or complex. The cost is obviously that the number of free parameters is increased.

To do this we accept the best-fitting models for each of the five regions and use these parameters as a starting point. However, additional parameters are included to allow α to vary independently for each velocity component. Optimization is done using `VPFIT`. In other words, we do not recommence the entire `AI-VPFIT` fitting process from scratch. The whole absorption complex (i.e. all five regions illustrated in Fig. 4) comprises a total of 62 velocity components for the LFC-calibrated spectrum (63 for the ThAr-calibrated). An initial trial fit showed that some badly-blended (and/or weak) velocity components provided only very poor constraints. In those cases we grouped components on small scales, resulting in a total of 47 individual measurements of $\Delta\alpha/\alpha$.

The 47 $\Delta\alpha/\alpha$ measurements obtained this way are shown in Fig. 6 for both the LFC (top panel) and the ThAr (middle panel) models. The weighted average $\Delta\alpha/\alpha$ across each of the five regions is tabulated in Table 3, together with their statistical uncertainties. The results are in good agreement with the results obtained previously, i.e. the weighted average of $\Delta\alpha/\alpha$ measurements within each region falls within 1σ of the results in Section 3.3.

Unlike the results obtained in Section 3.3, the weighted average over the 47 measurements for the LFC-calibrated spectrum ($\Delta\alpha/\alpha = -0.18 \pm 2.11 \times 10^{-6}$) and for the ThAr-calibrated spectrum ($\Delta\alpha/\alpha = 0.88 \pm 1.99 \times 10^{-6}$) are consistent with each other. As expected,

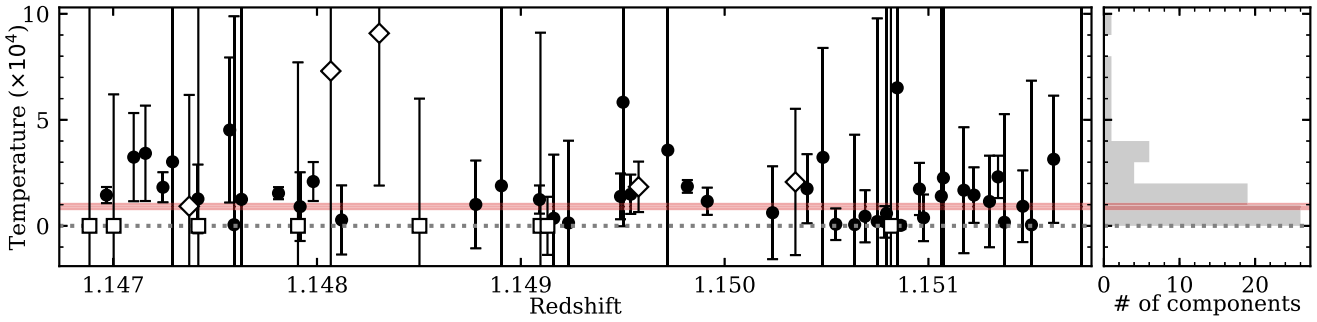

Figure 5. Temperatures of individual absorption components. Error bars represent 1σ uncertainties from the covariance matrix at the best-fitting solution. Black filled circles show components having both thermal and turbulent broadening. Thermal-only fits are marked by white diamonds. Turbulent-only fits are shown as white squares. The red shaded area marks the weighted average temperature, $T = 9.12 \pm 1.08 \times 10^3$ K. Individual measurements are scattered around this value with $\chi^2_\nu = 1.042$, where $\nu = 61$. The panel to the right is the histogram of temperatures.

Table 2. Measurements when a single $\Delta\alpha/\alpha$ parameter is used per region (Section 3.3), tabulated separately for the LFC and the ThAr models. Column 1 indicates the spectral region (see Fig. 4). Columns 2 and 3 give the number of metal components (N_c) and the number of free parameters (N_p) in each model. The average redshift of the metal components is in column 4. Columns 5 and 6 give the values of $\Delta\alpha/\alpha$ and their 1σ uncertainties from the best-fitting covariance matrix, respectively. Both are in units 10^{-6}. The normalized χ^2_ν for the fit is in column 7. The lower row gives the average over all five regions for the relevant quantities.

LFC						
ID	N_c	N_p	$\langle z \rangle$	$\frac{\Delta\alpha}{\alpha}$	σ_{stat}	χ^2_ν
I	13	125	1.14708	−3.90	4.42	0.9892
II	6	68	1.14788	17.74	4.30	0.9859
III	10	125	1.14870	18.45	15.07	0.9836
IV	7	89	1.14983	−6.39	4.12	0.8595
V	26	267	1.15080	−2.59	3.37	0.9860
All	62		1.14936	0.94	1.97	

ThAr						
ID	N_c	N_p	$\langle z \rangle$	$\frac{\Delta\alpha}{\alpha}$	σ_{stat}	χ^2_ν
I	14	134	1.14735	14.68	4.13	0.9652
II	6	68	1.14788	18.03	4.27	0.9730
III	10	116	1.14872	4.71	15.67	0.9662
IV	7	95	1.14984	−3.04	4.15	0.8343
V	26	245	1.15078	−2.89	3.12	0.9868
All	63		1.14949	4.82	1.92	

given the large number of free model parameters, there is generally a slight increase in the $\Delta\alpha/\alpha$ error estimates (compare Tables 2 and 3).

3.5 Consistency between 47 α measurements

We now explore the differences between the LFC and ThAr models in more detail. We bin the individual $\Delta\alpha/\alpha$ measurements in redshift bins $\Delta z = 1 \times 10^{-4}$ (the 47 measurements fall into 37 bins) and calculate the weighted average in each. Their differences (LFC minus ThAr) are illustrated in the lower panel of Fig. 6. The LFC and ThAr measurements agree well everywhere except in region I. Most of the LFC-ThAr differences in region I are located around -2×10^{-5}, with two bins (at the high-redshift end) at more negative values (-1.8 and -7.6×10^{-4}). The top two panels of Fig. 6 suggest this is caused by velocity structure differences between the LFC and ThAr models. Discarding the points in these two bins and taking the weighted average of the remaining points in region I, we get $-4.90 \pm 5.49 \times 10^{-6}$ for LFC and $15.68 \pm 8.54 \times 10^{-6}$ for ThAr, i.e. the two remain inconsistent.

The most significant deviation from zero occurs in region II ($\approx 3\sigma$). Measurements from the LFC-calibrated and the ThAr-calibrated spectrum are in excellent agreement in this region.

A substantial advantage of deriving $\Delta\alpha/\alpha$ measurements for individual absorbing components (or small groups) is that it may help to identify and filter out any possible rogue measurements. The least trimmed squares (LTS) method is frequently used for this and provides a more robust estimate of the mean. We thus apply LTS here, discarding 15 per cent of the data in each region. The discarded components are listed in column 6 of Table 3. The weighted averages for each region and the entire sample after LTS trimming are tabulated in columns 7 and 8 of the same table. Interestingly, the consequence of removing the most outlying measurement in region II was to move the region's average towards more positive values (but doubling the error and therefore making the result less significant).

The measured scatter (i.e. the empirical standard deviation) of the remaining 40 LFC-calibrated measurements is $\sigma = 9 \times 10^{-5}$. This is slightly smaller than the average error on individual measurements, $\langle \sigma^{stat} \rangle = 14 \times 10^{-5}$. The scatter of the ThAr-calibrated measurements is $\sigma = 13 \times 10^{-5}$ (the same as the average error).

3.6 Consistency with previous studies

Recently, a detailed study of this same absorption complex was carried out (Kotuš et al. 2017) using spectra from the UVES spectrograph (Dekker et al. 2000) on the Very Large Telescope. Those spectra are higher S/N although the spectral resolution is lower. Comparing with those results reveals good consistency. In this paper we split the data into five distinct regions whereas Kotuš et al. (2017) use three. However, combining our regions {I+II} ('left') and {III + IV} ('centre') enables the comparison (our region V corresponds to Kotuš' 'right' region). Using the $\Delta\alpha/\alpha$ results from the LTS trimmed sample in our Table 3 (LFC-calibrated) and Kotuš' table 4, and combining all random and systematic errors appropriately, the $\Delta\alpha/\alpha$ solution differ by 1.15σ, 1.02σ, and 0.92σ respectively, left to right.

Prior to our study, Kotuš et al. (2017) was the most detailed study. However, several prior analyses also exist (Quast et al. 2004; Levshakov et al. 2005, 2006; Chand et al. 2006; Molaro et al. 2008). All produced results consistent with no change in α, with somewhat larger uncertainties than derived from our analysis or that of Kotuš et al. (2017).

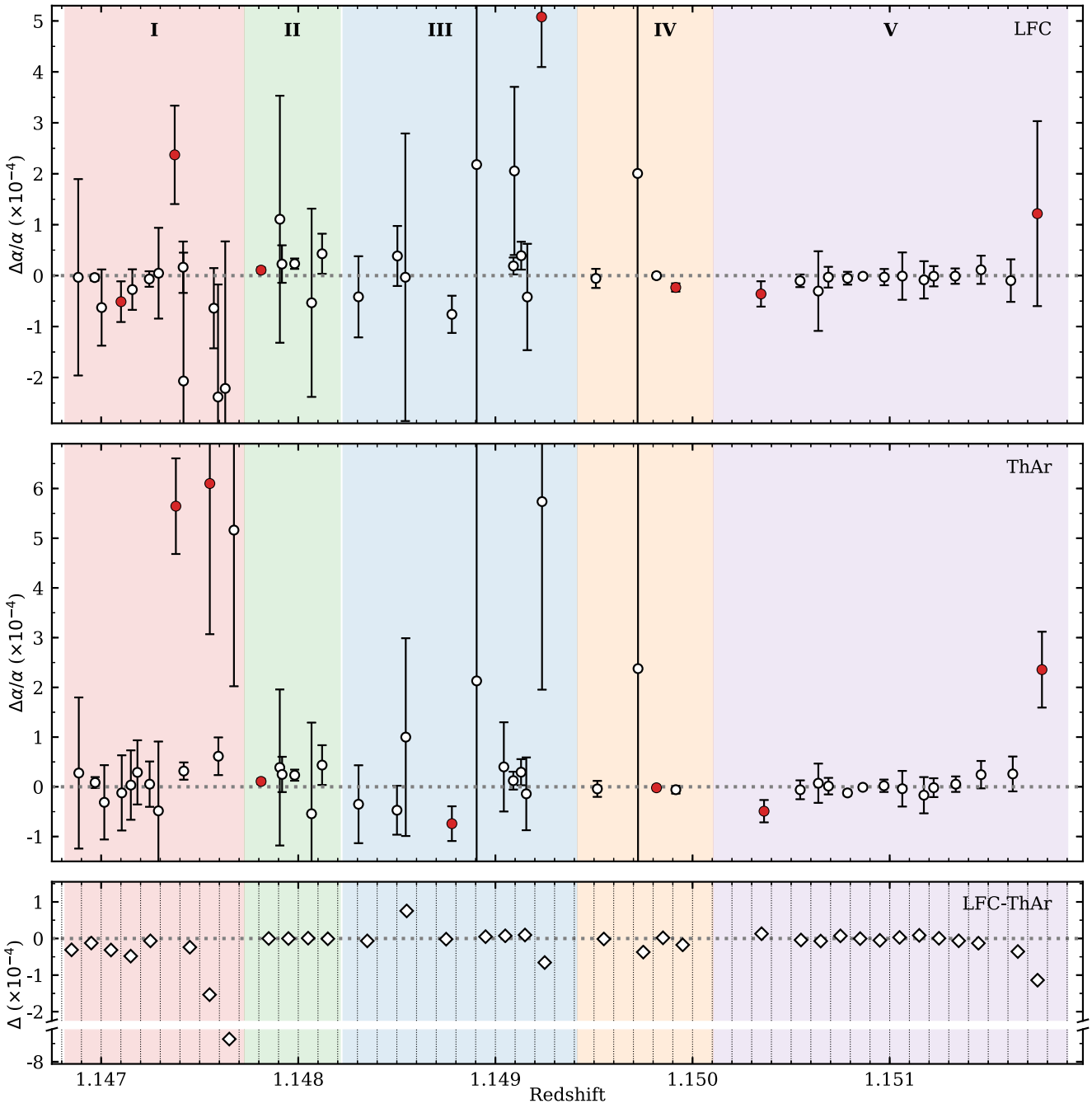

Figure 6. The 47 $\Delta\alpha/\alpha$ measurements. Some components were grouped together (Section 3.4). Measurements from the LFC-calibrated spectrum are shown in the top panel. ThAr results are shown in the middle panel. The lower panel shows the difference between the LFC and the ThAr measurements after averaging in bins of $\Delta z = 1 \times 10^{-4}$ (vertical dotted lines). Weighted averages of points in each region are tabulated in Table 3. Filled red circles indicate measurements removed by least trimmed squares. The weighted averages for each region, after discarding those points, are also given in Table 3. The data illustrated in the top two panels are available as online supplementary material.

4 RESULTS

Fig. 7 shows the $\Delta\alpha/\alpha$ measurements tabulated in Tables 2 and 3. The two large panels show the results from the LFC-calibrated (top panel) and the ThAr-calibrated spectrum (bottom panel). The weighted average for the entire $z \approx 1.15$ absorption complex are plotted in the small panels to the right of the main panels. Our main results are summarized as follows:

(i) In the analysis presented in Section 3.3, we obtain five $\Delta\alpha/\alpha$ measurement (one per region) from the LFC-calibrated and from the ThAr-calibrated spectrum independently. For the LFC-calibrated spectrum, the average over the five regions is consistent with no variation in α. Applying the same methods to the ThAr calibrated spectrum, we obtain a 2.5σ deviation from zero. These results are tabulated in Table 2 and plotted as black points in Fig. 7.

Table 3. The weighted average of the 47 individual $\Delta\alpha/\alpha$ measurements, grouped by region. Column 1 identifies the spectral region. Column 2 gives the total number of $\Delta\alpha/\alpha$ measurements in the region. Column 3 gives the weighted average redshift. Column 4 and 5 give the weighted average $\Delta\alpha/\alpha$ and associated error on the mean in units 1×10^{-6}. Column 6 indicates which absorption components were LTS trimmed (see figures in Appendices B and C). Columns 7 and 8 give the weighted average $\Delta\alpha/\alpha$ and uncertainty after applying LTS. The lower row provides weighted averages over all 47 measurements (40 after LTS). Superscripts in Column 2 and below the table identify which absorption components were removed by LTS. Where a component lies in a group, the entire group was discarded.

			LFC				
ID	N	$\langle z \rangle$	$\langle \frac{\Delta\alpha}{\alpha} \rangle$	$\sigma_{\rm stat}$	LTS	$\langle \frac{\Delta\alpha}{\alpha} \rangle_{\rm LTS}$	$\sigma^{\rm LTS}_{\rm stat}$
I	13	1.14707	−5.40	5.47	ap,au	−5.32	5.53
II	6	1.14784	14.17	4.71	ac	24.45	9.51
III	10	1.14877	19.51	12.48	au	11.53	12.58
IV	4[a]	1.14984	−6.77	4.25	aj	−0.50	5.00
V	14[b]	1.15077	−2.98	3.45	ab,ar	−2.38	3.48
All	47	1.14943	−0.18	2.11		−0.27	2.41
			ThAr				
ID	N	$\langle z \rangle$	$\langle \frac{\Delta\alpha}{\alpha} \rangle$	$\sigma_{\rm stat}$	LTS	$\langle \frac{\Delta\alpha}{\alpha} \rangle_{\rm LTS}$	$\sigma^{\rm LTS}_{\rm stat}$
I	13[c]	1.14732	21.22	8.51	aw,ar	16.47	8.55
II	6	1.14784	13.72	4.69	ac	24.67	10.23
III	10	1.14871	0.72	12.60	al	11.92	13.51
IV	4[d]	1.14984	−3.08	3.89	ae	−5.52	7.02
V	14[e]	1.15078	−4.10	2.87	as,ax	−3.70	2.90
All	47	1.14957	0.88	1.99		−0.15	2.44

Notes. [a]Grouped: (ag,am,aa,al).
[b]Grouped: (ab,aj,al,bm), (bs,bi,ah,ac), (ak,ao), (bq,bc), (ag,an), (ai,as,am), (au,bo).
[c]Grouped: (at,aa).
[d]Grouped: (ag,ak,aa,am).
[e]Grouped: (as,bd,ah,bo), (at,aq), (ao,ay,ab), (ak,bg), (an,bq), (ag,ad), (ai,bc,bi), (ap,bm).

(ii) Including $\Delta\alpha/\alpha$ as a free parameter for 47 individual absorption components (or appropriately grouped components) allows us to identify regions of data significantly affecting the overall measurement (Section 3.4). These results, tabulated in Table 3 and plotted as red squares on Fig. 7, are in excellent agreement with the results from Section 3.3.

(iii) To explore robustness, we apply LTS, removing 15 per cent of the sample in each region, obtaining the results plotted as green diamonds in Fig. 7. This reduces the total number of measurements to 40. The weighted average over the 40 measurements is consistent with zero for both calibrations: $\Delta\alpha/\alpha = -0.27 \pm 2.41 \times 10^{-6}$ (LFC) and $\Delta\alpha/\alpha = -0.15 \pm 2.44 \times 10^{-6}$ (ThAr).

(iv) When using the approach in Section 3.3, the wavelength scale distortions imparted by the ThAr calibration methods (see Fig. 1) have a small, but measurable, effect. The same distortions appear to have no effect on the measurements in Section 3.4.

(v) The HE0515−4414 absorption complex modelled spans approximately 700 km s^{-1}. If this system represents a line of sight through a cluster of order 1 Mpc across, we can place an upper limit, for the first time, on small-scale α variations, using the empirical scatter in the 40 $\Delta\alpha/\alpha$ measurements. The upper limit on small-scale α variations over scale lengths ≈25 kpc, is ≈9×10^{-5} (Section 3.5).

(vi) Averaged over all absorption components, we derive a gas temperature of $T = 9.12 \pm 1.08 \times 10^3$ K (Section 3.2). This value is in agreement with the results from Carswell et al. (2012) who found $T = 12 \pm 3 \times 10^3$ K in a quasar absorption system at $z_{\rm abs} = 2.076$. As seen, the new data presented in this paper provide a more stringent constraint and also suggest that all individual absorption components are consistent with a single gas temperature.

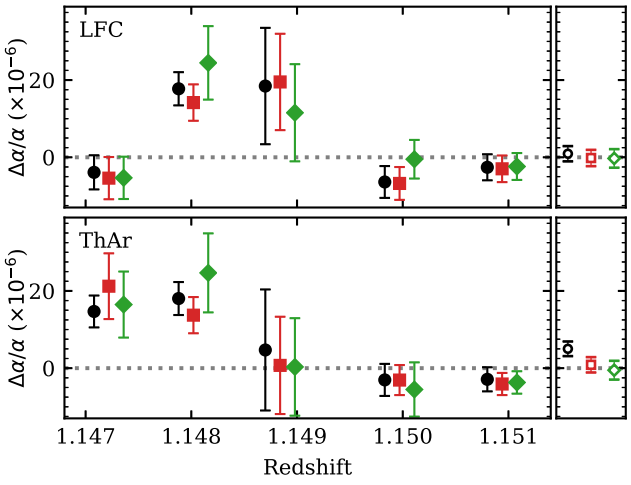

Figure 7. Comparing the different approaches to measuring α from the LFC-calibrated spectrum (top) and the ThAr-calibrated spectrum (bottom). Measurements from Section 3.3 are shown as black points. The weighted average of the 47 measurements, derived in Section 3.4, are shown as red squares. The green diamonds are after outlier removal. Points were offset along the x-axis for clarity. Panels on the right show the weighted average over the entire absorption complex.

5 DISCUSSION

In this work we have analysed the first LFC-calibrated quasar spectrum. Quasar spectra of similar quality to the one presented here will be routinely produced by the new ESPRESSO spectrograph installed on the Very Large Telescope (Pepe et al. 2014) and by the future HIRES instrument on the Extremely Large Telescope (Maiolino et al. 2013). Both of these instruments have LFCs for wavelength calibration. We hope that the new methods introduced in this paper will be beneficial in analysing future observations.

We have demonstrated that careful modelling procedures play a crucial part in the analysis of high-resolution spectroscopic data. Tools such as `AI-VPFIT` eliminate any potential human bias and yield optimal models of the data in a reproducible and objective manner.

Choosing the correct line broadening mechanism, i.e. including temperature parameters for individual components, is important. Models produced assuming an incorrect broadening mechanism tend to generate artificial close blends of absorption lines. Modelling simulated data, based on the HE0515 spectrum used in this work, shows that using an incorrect broadening mechanism biases α measurements (Lee et al. 2020).

Examining the scatter of the five measurements obtained from the LFC-calibrated spectrum in Section 3.3, we find they have $\chi^2 = 21.99$ ($\nu = 4$) . For a χ^2 distribution with four degrees of freedom, the probability of observing χ^2 values at least this large is $p = 0.02$ per cent. The five measurements are therefore highly inconsistent with each other. Performing the same for the 47 measurements from Section 3.4, we find the LFC-calibrated measurements have a $\chi^2 = 72.86$ ($\nu = 46$, $p = 0.7$ per cent). We assume this is not caused by small-scale spatial variations in α across the redshift range covered by the absorption system. After LTS trimming, the scatter in the remaining 40 measurements are

consistent with their individually estimated errors ($\chi^2 = 23.76$, $\nu = 39$, $p = 97$ per cent). Similar results are obtained for the ThAr spectrum.

The analysis presented here is based on the assumption of solar relative isotopic abundances. Significant deviations from solar values translate to large shifts in $\Delta\alpha/\alpha$ (Webb et al. 1999; Ashenfelter, Mathews & Olive 2004a, b; Fenner, Murphy & Gibson 2005; Berengut, Kava & Flambaum 2012; Webb et al. 2014). Very approximately, when simultaneously modelling Mg II and Fe II, the measured $\Delta\alpha/\alpha$ may shift towards negative values by as much as $\approx 5 \times 10^{-6}$ for 100 per cent ^{24}Mg and by the same amount in the positive direction for 100 per cent $^{25+26}$Mg. A discussion as to the validity of the solar isotopic assumption is deferred to a subsequent paper.

For these particular observations, LFC calibration methods have not yielded significantly different $\Delta\alpha/\alpha$ measurements compared to the ThAr methods. The probable reason for this lies in the fact that we have combined a large number of individual exposures to form a final co-added spectrum. Due to different barycentric velocities for each observation, the position of relevant transitions falls differently with respect to the complicated distortion pattern each time, effectively smearing it out. This is less likely to occur for more efficient spectrographs, such as ESPRESSO and HIRES.

ACKNOWLEDGEMENTS

We wish to dedicate this work to our dear colleague and friend John Barrow, who has played such an important role in the development of this subject. Based on observations collected at the European Organisation for Astronomical Research in the Southern Hemisphere under ESO programme 102.A-0697(A). We are grateful for the award of computing time for this research on the gStar and OzStar supercomputing facilities at the Centre for Astrophysics and Supercomputing, Swinburne University of Technology. DM thanks Prashin Jethwa for useful discussions during the early stages of the analysis. JKW thanks the John Templeton Foundation, the Department of Applied Mathematics and Theoretical Physics and the Institute of Astronomy at Cambridge University for hospitality and support, and Clare Hall for a Visiting Fellowship during this work. We thank the referee for their useful comments.

DATA AVAILABILITY

We provide as online supplementary material: (i) the LFC and ThAr wavelength calibrated co-added spectra, (ii) the final models, and (iii) all input files for `VPFIT` and `AI-VPFIT`, including atomic data.

REFERENCES

Akaike H., 1974, IEEE Trans. Autom. Control, 19, 716
Aldenius M., 2009, Phys. Scr. T, 134, 014008
Andersen T., Desesquelles J., Jessen K. A., Sørensen G., 1970, Phys. Rev. A, 1, 1294
Ansbacher W., Li Y., Pinnington E. H., 1989, Phys. Lett. A, 139, 165
Ashenfelter T., Mathews G. J., Olive K. A., 2004a, Phys. Rev. Lett., 92, 041102
Ashenfelter T. P., Mathews G. J., Olive K. A., 2004b, ApJ, 615, 82
Asplund M., Grevesse N., Sauval A. J., Scott P., 2009, ARA&A, 47, 481
Avelino P. P. et al., 2001, Phys. Rev. D, 64, 103505
Bahcall J. N., Steinhardt C. L., Schlegel D., 2004, ApJ, 600, 520
Bainbridge M. et al., 2017, Universe, 3, 32
Bainbridge M. B., Webb J. K., 2017, MNRAS, 468, 1639
Barrow J. D., Lip S. Z. W., 2012, Phys. Rev. D, 85, 023514
Batteiger V. et al., 2009, Phys. Rev. A, 80, 022503
Bekenstein J. D., 1982, Phys. Rev. D, 25, 1527
Berengut J. C., Dzuba V. A., Flambaum V. V., Marchenko M. V., 2004, Phys. Rev. A, 70, 064101
Berengut J. C., Flambaum V. V., Kozlov M. G., 2005, Phys. Rev. A, 72, 044501
Berengut J. C., Kava E. M., Flambaum V. V., 2012, A&A, 542, A118
Berengut J. C., Flambaum V. V., Ong A., Webb J. K., Barrow J. D., Barstow M. A., Preval S. P., Holberg J. B., 2013, Phys. Rev. Lett., 111, 010801
Bielby R., Crighton N. H. M., Fumagalli M., Morris S. L., Stott J. P., Tejos N., Cantalupo S., 2017, MNRAS, 468, 1373
Biemont E., Baudoux M., Kurucz R. L., Ansbacher W., Pinnington E. H., 1991, A&A, 249, 539
Blackwell-Whitehead R. J., Toner A., Hibbert A., Webb J., Ivarsson S., 2005, MNRAS, 364, 705
Bretagnon P., Francou G., 1988, A&A, 202, 309
Carswell R. F., Becker G. D., Jorgenson R. A., Murphy M. T., Wolfe A. M., 2012, MNRAS, 422, 1700
Chand H., Srianand R., Petitjean P., Aracil B., Quast R., Reimers D., 2006, A&A, 451, 45
Copeland E. J., Nunes N. J., Pospelov M., 2004, Phys. Rev. D, 69, 023501
Damour T., Dyson F., 1996, Nucl. Phys. B, 480, 37
Dekker H., D'Odorico S., Kaufer A., Delabre B., Kotzlowski H., 2000, in Iye M., Moorwood A. F., eds, Proc. SPIE Conf. Ser. Vol. 4008, Optical and IR Telescope Instrumentation and Detectors. SPIE, Bellingham, p. 534
Dicke R. H., 1959, Nature, 183, 170
Dumont V., Webb J. K., 2017, MNRAS, 468, 1568
Dzuba V. A., Flambaum V. V., 2009, Can. J. Phys., 87, 15
Dzuba V. A., Johnson W. R., 2007, Phys. Rev. A, 76, 062510
Dzuba V. A., Flambaum V. V., Webb J. K., 1999a, Phys. Rev. A, 59, 230
Dzuba V. A., Flambaum V. V., Webb J. K., 1999b, Phys. Rev. Lett., 82, 888
Dzuba V. A., Flambaum V. V., Kozlov M. G., Marchenko M., 2002, Phys. Rev. A, 66, 022501
Evans T. M. et al., 2014, MNRAS, 445, 128
Fenner Y., Murphy M. T., Gibson B. K., 2005, MNRAS, 358, 468
Griest K., Whitmore J. B., Wolfe A. M., Prochaska J. X., Howk J. C., Marcy G. W., 2010, ApJ, 708, 158
Guo B., Ansbacher W., Pinnington E. H., Ji Q., Berends R. W., 1992, Phys. Rev. A, 46, 641
Hänsch T. W., 2006, Rev. Mod. Phys., 78, 1297
Hees A. et al., 2020, Phys. Rev. Lett., 124, 081101
Horne K., 1986, PASP, 98, 609
Itano W. M., Wineland D. J., 1981, Phys. Rev. A, 24, 1364
Kelly F. M., Mathur M. S., 1978, Can. J. Phys., 56, 1422
King J. A., Webb J. K., Murphy M. T., Flambaum V. V., Carswell R. F., Bainbridge M. B., Wilczynska M. R., Koch F. E., 2012, MNRAS, 422, 3370
Kling R., Griesmann U., 2000, ApJ, 531, 1173
Kotuš S. M., Murphy M. T., Carswell R. F., 2017, MNRAS, 464, 3679
Kwiatkowski M., Micali G., Werner K., Zimmermann P., 1982, J. Phys. B, 15, 4357
Larsson J., Zerne R., Persson A., Wahlström C. G., Svanberg S., 1993, Z. Phys. D, 27, 329
Lee C.-C., Webb J. K., Carswell R. F., Milaković D., 2020, MNRAS, preprint (arXiv:2008.02583)
Levshakov S. A., Centurión M., Molaro P., D'Odorico S., 2005, A&A, 434, 827
Levshakov S. A., Centurión M., Molaro P., D'Odorico S., Reimers D., Quast R., Pollmann M., 2006, A&A, 449, 879
Liljeby L., Lindgård A., Mannervik S., Veje E., Jelenkovic B., 1980, Phys. Scr., 21, 805
Lo Curto G. et al., 2015, The Messenger, 162, 9
Lundin L., Engman B., Hilke J., Martinson I., 1973, Phys. Scr., 8, 274
Lurio A., 1964, Phys. Rev., 136, 376
Maiolino R. et al., 2013, preprint (arXiv:1310.3163)
Marek J., Richter J., 1973, A&A, 26, 155
Marra V., Rosati F., 2005, J. Cosmol. Astropart. Phys., 2005, 011
Martins C. J. A. P., 2017, Rep. Prog. Phys., 80, 126902
Mayor M. et al., 2003, The Messenger, 114, 20

Milaković D., Pasquini L., Webb J. K., Lo Curto G., 2020, MNRAS, 493, 3997
Molaro P. et al., 2013, A&A, 560, A61
Molaro P., Reimers D., Agafonova I. I., Levshakov S. A., 2008, Eur. Phys. J. Spec. Top., 163, 173
Mota D. F., Barrow J. D., 2004a, MNRAS, 349, 291
Mota D. F., Barrow J. D., 2004b, Phys. Lett. B, 581, 141
Murphy M. T., Berengut J. C., 2014, MNRAS, 438, 388
Murphy M. T., Webb J. K., Flambaum V. V., 2003, MNRAS, 345, 609
Nave G., 2012, MNRAS, 420, 1570
Olive K. A., Pospelov M., 2002, Phys. Rev. D, 65, 085044
Pepe F. et al., 2014, Astron. Nachr., 335, 8
Pinnington E. H., Guo G., Ji Q., Berends R. W., Ansbacher W., Biemont E., 1992, J. Phys. B, 25, L475
Planck Collaboration et al., 2015, A&A, 580, A22
Porsev S. G., Kozlov M. G., Reimers D., 2009, Phys. Rev. A, 79, 032519
Probst R. A. et al., 2020, Nat. Astron., 4, 603
Quast R., Reimers D., Levshakov S. A., 2004, A&A, 415, L7
Rahmani H. et al., 2013, MNRAS, 435, 861
Reimers D., Hagen H.-J., Rodriguez-Pascual P., Wisotzki L., 1998, A&A, 334, 96
Robertson J. G., 1986, PASP, 98, 1220
Rodler F., Lo Curto G., 2019, HARPS User Manual. European Southern Observatory, 2.3 edn. Available at: https://www.eso.org/sci/facilities/lasilla/instruments/harps/doc/manual/HARPS-UserManual2.3.pdf
Rosenband T. et al., 2008, Science, 319, 1808
Rosman K. J. R., Taylor P. D. P., 1998, J. Phys. Chem. Ref. Data, 27, 1275
Salumbides E. J., Hannemann S., Eikema K. S. E., Ubachs W., 2006, MNRAS, 373, L41
Sandvik H. B., Barrow J. D., Magueijo J., 2002, Phys. Rev. Lett., 88, 031302
Savukov I. M., Dzuba V. A., 2008, Phys. Rev. A, 77, 042501
Schade W., Mundt B., Helbig V., 1988, J. Phys. B, 21, 2691
Schnabel R., Bard A., Kock M., 1995, Z. Phys. D, 34, 223
Shaw D. J., Barrow J. D., 2005, Phys. Rev. D, 71, 063525
Silva M. F., Winther H. A., Mota D. F., Martins C. J. A. P., 2014, Phys. Rev. D, 89, 024025
Smith W. W., Gallagher A., 1966, Phys. Rev., 145, 26
Smith W. H., Liszt H. S., 1971, J. Opt. Soc. Am., 61, 938
Stadnik Y. V., Flambaum V. V., 2015, Phys. Rev. Lett., 115, 201301
Steinmetz T. et al., 2008, Science, 321, 1335
Sugiura N., 1978, Commun. Stat. - Theory Methods, 7, 13
Sur C., Sahoo B. K., Chaudhuri R. K., Das B. P., Mukherjee D., 2005, Eur. Phys. J. D, 32, 25
Ubachs W., 2018, Space Sci. Rev., 214, 3
Udem T., Holzwarth R., Hänsch T. W., 2002, Nature, 416, 233
Uzan J.-P., 2011, Living Rev. Relat., 14, 2
Webb J. K., Flambaum V. V., Churchill C. W., Drinkwater M. J., Barrow J. D., 1999, Phys. Rev. Lett., 82, 884
Webb J. K., King J. A., Murphy M. T., Flambaum V. V., Carswell R. F., Bainbridge M. B., 2011, Phys. Rev. Lett., 107, 191101
Webb J. K., Wright A., Koch F. E., Murphy M. T., 2014, Mem. Soc. Astron. Ital., 85, 57
Whitmore J. B., Murphy M. T., 2015, MNRAS, 447, 446
Whitmore J. B., Murphy M. T., Griest K., 2010, ApJ, 723, 89
Wilczynska M. R. et al., 2020, Sci. Adv., 6, eaay9672
Wilczynska M. R., Webb J. K., King J. A., Murphy M. T., Bainbridge M. B., Flambaum V. V., 2015, MNRAS, 454, 3082
Wilken T. et al., 2010, MNRAS, 405, L16

SUPPORTING INFORMATION

Supplementary data are available at *MNRAS* online.

supplementary_material

Please note: Oxford University Press is not responsible for the content or functionality of any supporting materials supplied by the authors. Any queries (other than missing material) should be directed to the corresponding author for the article.

APPENDIX A: ATOMIC DATA

Table A1. Atomic species and transitions, with isotopic structure, used in this analysis. Terrestrial isotopic relative abundances are assumed. Column 4 (λ_0) is rest-frame wavelength. Column 5 (f) is oscillator strength or relative abundance (per cent). The latter are from Rosman & Taylor (1998). Column 6 (Γ) is the sum of the spontaneous emission rates. Column 7 (q) gives the sensitivity coefficients to a change in the fine structure constant α. Citations to original measurement papers are given at the foot of the table. An atomic data compilation including the data in this table is given in Murphy & Berengut (2014).

Ion	Tran.	A	λ_0 (Å)	f or per cent	Γ (10^8 s^{-1})	q (cm^{-1})
Fe II	2344	55.845	2344.212747(76)[a, b]	0.114	2.680[c, d]	1375[e, f](300)
		58	2344.2113616[f]	0.282 per cent		
		57	2344.2120103[f]	2.119 per cent		
		56	2344.2126822[f]	91.754 per cent		
		54	2344.2141007[f]	5.845 per cent		
	2374	55.845	2374.460064(78)[a, b]	0.03130	3.090[c, g]	1625[e, f](100)
		58	2374.4582998[f]	0.282 per cent		
		57	2374.4591258[f]	2.119 per cent		
		56	2374.4599813[f]	91.754 per cent		
		54	2374.4617873[f]	5.845 per cent		
	2382	55.845	2382.763995(80)[a, b]	0.320	3.130[c, g]	1505[e, f](100)
		58	2382.7622294[f]	0.282 per cent		
		57	2382.7630560[f]	2.119 per cent		
		56	2382.7639122[f]	91.754 per cent		
		54	2382.7657196[f]	5.845 per cent		
	2586	55.845	2586.649312(87)[a, b]	0.0691	2.720[c]	1515[e, f](100)

Table A1 – *continued*

Ion	Tran.	A	λ_0 (Å)	f or per cent	Γ (10^8 s^{-1})	q (cm^{-1})
		58	2586.6475648[f]	0.282 per cent		
		57	2586.6483830[f]	2.119 per cent		
		56	2586.6492304[f]	91.754 per cent		
		54	2586.6510194[f]	5.845 per cent		
	2600	55.845	2600.172114(88)[a, g]	0.239	2.700[c]	1370[e, f](100)
		58	2600.1703603[f]	0.282 per cent		
		57	2600.1711816[f]	2.119 per cent		
		56	2600.1720322[f]	91.754 per cent		
		54	2600.1738281[f]	5.845 per cent		
Mg I	2852	24.3050	2852.962797(15)	1.83	$5.000^{h,i,j,k,l}_{m,n,o,p}$	90[q, r](10)
		26	2852.959591(20)[s]	11.01 per cent		
		25	2852.961407(20)[s]	10.00 per cent		
		24	2852.963420(14)[s]	78.99 per cent		
Mg II	2796	24.3050	2796.353790(16)	0.6155	2.625[t]	212[u](2)
		26	2796.34704565(42)[v]	11.01 per cent		
		25	2796.353449(50)[v, w, x]	4.17 per cent		
		25	2796.349030(50)[v, w, x]	5.83 per cent		
		24	2796.35509903(42)[v]	78.99 per cent		
	2803	24.3050	2803.530982(16)	0.3058	2.595[t]	121[u](2)
		26	2803.52420938(42)[v]	11.01 per cent		
		25	2803.530941(50)[v, w, x]	4.17 per cent		
		25	2803.525985(50)[v, w, x]	5.83 per cent		
		24	2803.53229720(42)[v]	78.99 per cent		
Mn II	2576	54.9380	2576.87512(11)[a, b, y]	0.361	2.820[z,A,B,C]	1276[D](150)
		55	2576.890898	28.571 per cent		
		55	2576.879368	23.801 per cent		
		55	2576.869849	19.030 per cent		
		55	2576.862494	14.286 per cent		
		55	2576.856181	14.312 per cent		
	2594	54.9380	2594.49643(11)[a, b, y]	0.280	2.780[z,A,B,C]	1030[D](150)
		55	2594.512068	28.579 per cent		
		55	2594.500587	23.841 per cent		
		55	2594.491191	19.078 per cent		
		55	2594.483901	14.289 per cent		
		55	2594.477608	14.213 per cent		
	2606	54.9380	2606.45877(11)[a, b, y]	0.198	2.270[z,A,B,C]	869[D](150)
		55	2606.478271	28.563 per cent		
		55	2606.463977	23.793 per cent		
		55	2606.452264	19.052 per cent		
		55	2606.443176	14.282 per cent		
		55	2606.435406	14.310 per cent		

Notes. [a]Aldenius (2009); [b]Nave (2012); [c]Biemont et al. (1991); [d]Guo et al. (1992); [e]Dzuba et al. (2002); [f]Porsev, Kozlov & Reimers (2009); [g]Schade, Mundt & Helbig (1988); [h]Lurio (1964); [i]Smith & Gallagher (1966); [j]Andersen et al. (1970); [k]Smith & Liszt (1971); [l]Lundin et al. (1973); [m]Marek & Richter (1973); [n]Kelly & Mathur (1978); [o]Liljeby et al. (1980); [p]Larsson et al. (1993); [q]Berengut, Flambaum & Kozlov (2005); [r]Savukov & Dzuba (2008); [s]Salumbides et al. (2006); [t]Ansbacher, Li & Pinnington (1989); [u]Dzuba & Johnson (2007); [v]Batteiger et al. (2009); [w]Itano & Wineland (1981); [x]Sur et al. (2005). [y]Blackwell-Whitehead et al. (2005); [z]Kwiatkowski et al. (1982); [A]Pinnington et al. (1992); [B]Schnabel, Bard & Kock (1995); [C]Kling & Griesmann (2000); [D]Berengut et al. (2004).

APPENDIX B: LFC-CALIBRATED MODELS

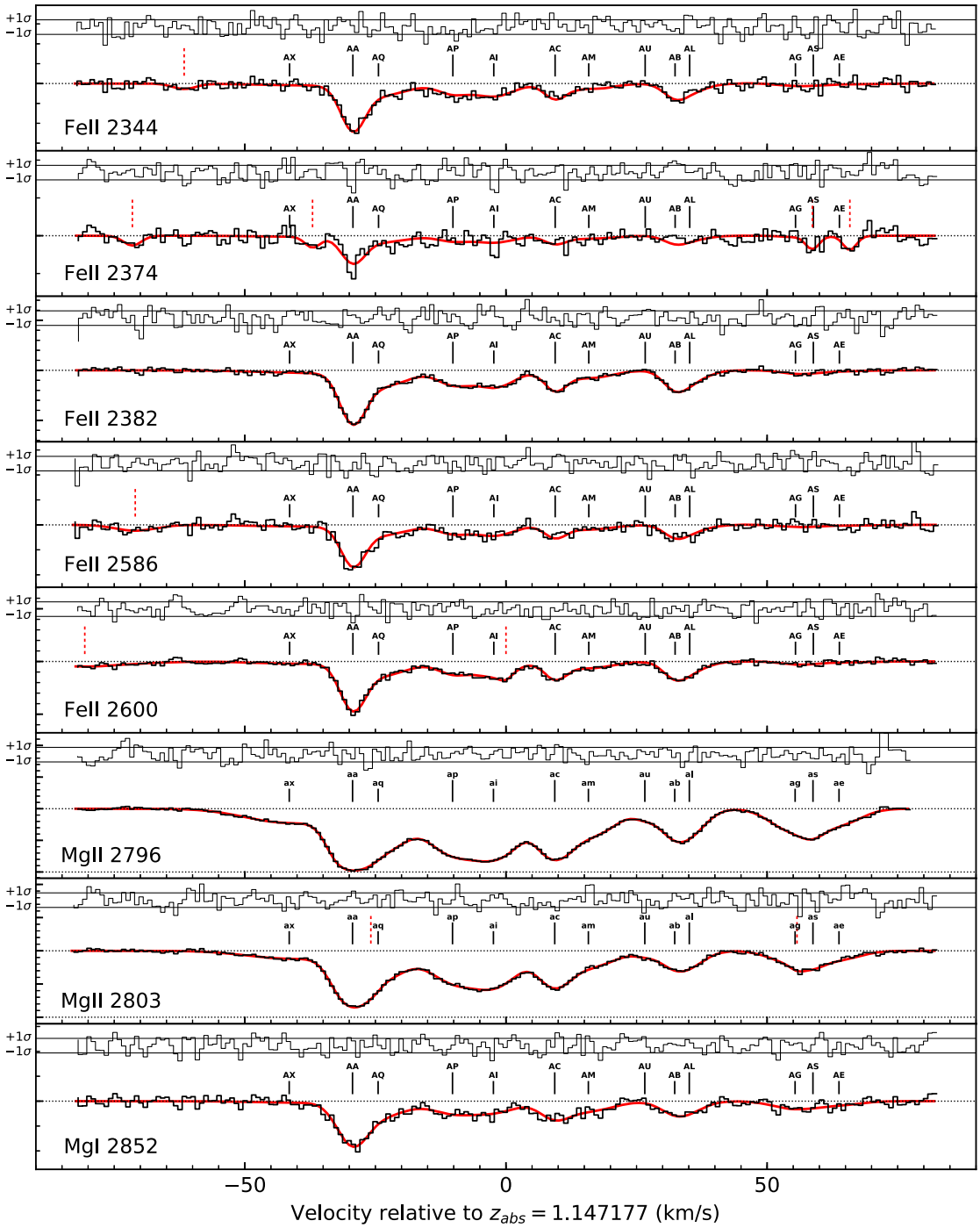

Figure B1. The black histogram shows the continuum-normalized LFC-calibrated spectrum for spectral region I. Overplotted as a continuous red line is the lowest AICc `AI-VPFIT` model. Black labelled ticks mark the locations of absorption components in the model. The lowercase letters are associated with the transitions that provide the most information about the velocity structure (i.e. the 'primary species', see Lee et al. 2020). Slightly longer, dotted red ticks mark the locations of blends from unidentified species (interlopers). The black histogram above the data and the model show the normalized residuals (data-model) and the horizontal lines show the $\pm 1\sigma$ levels. The dotted horizontal line corresponds to a normalized flux of unity. Major (minor) ticks on the y-axis label increments of 0.5 (0.1) in normalized flux.

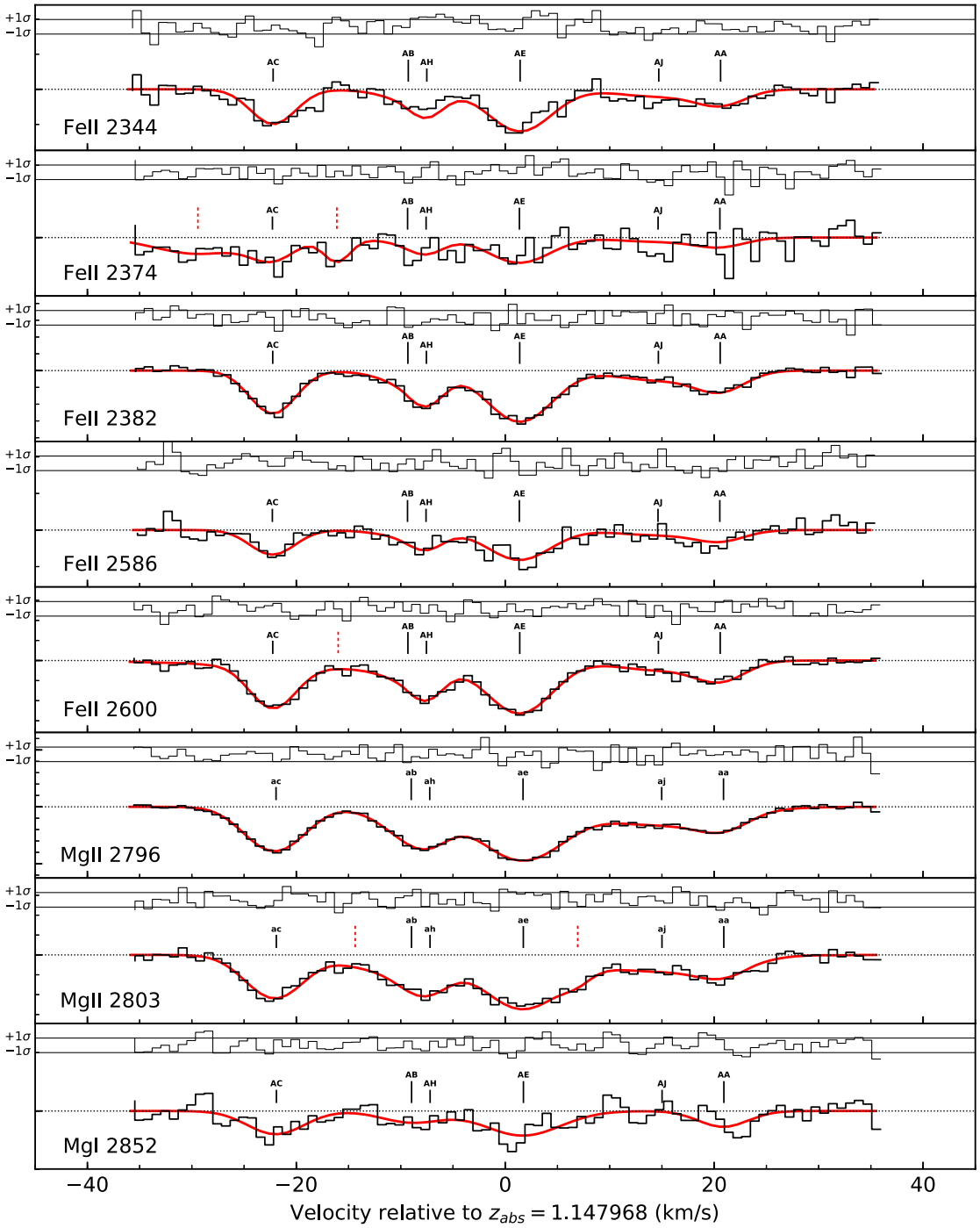

Figure B2. The same as in Fig. B1, except for LFC-calibrated spectral region II.

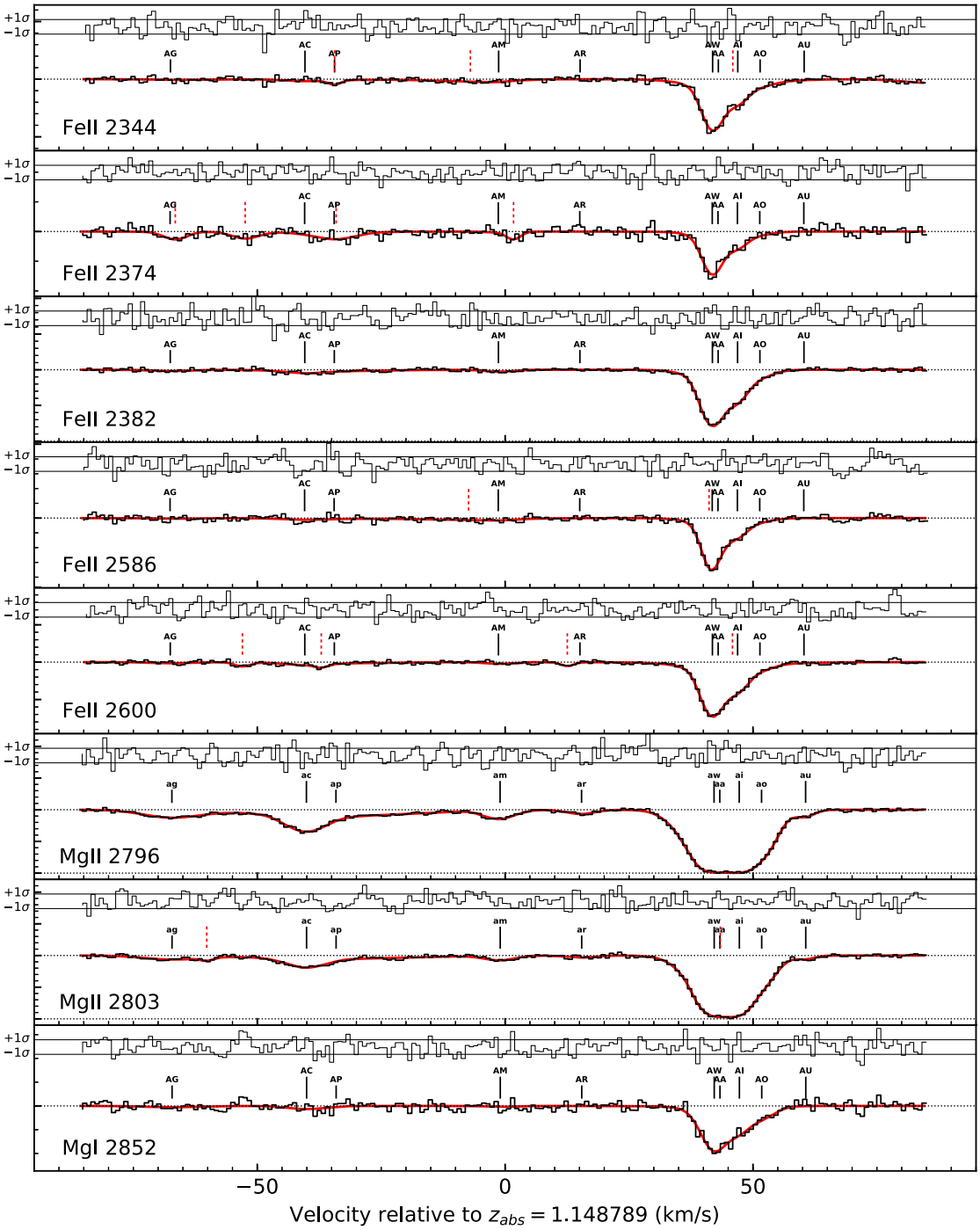

Figure B3. The same as in Fig. B1, except for LFC-calibrated spectral region III.

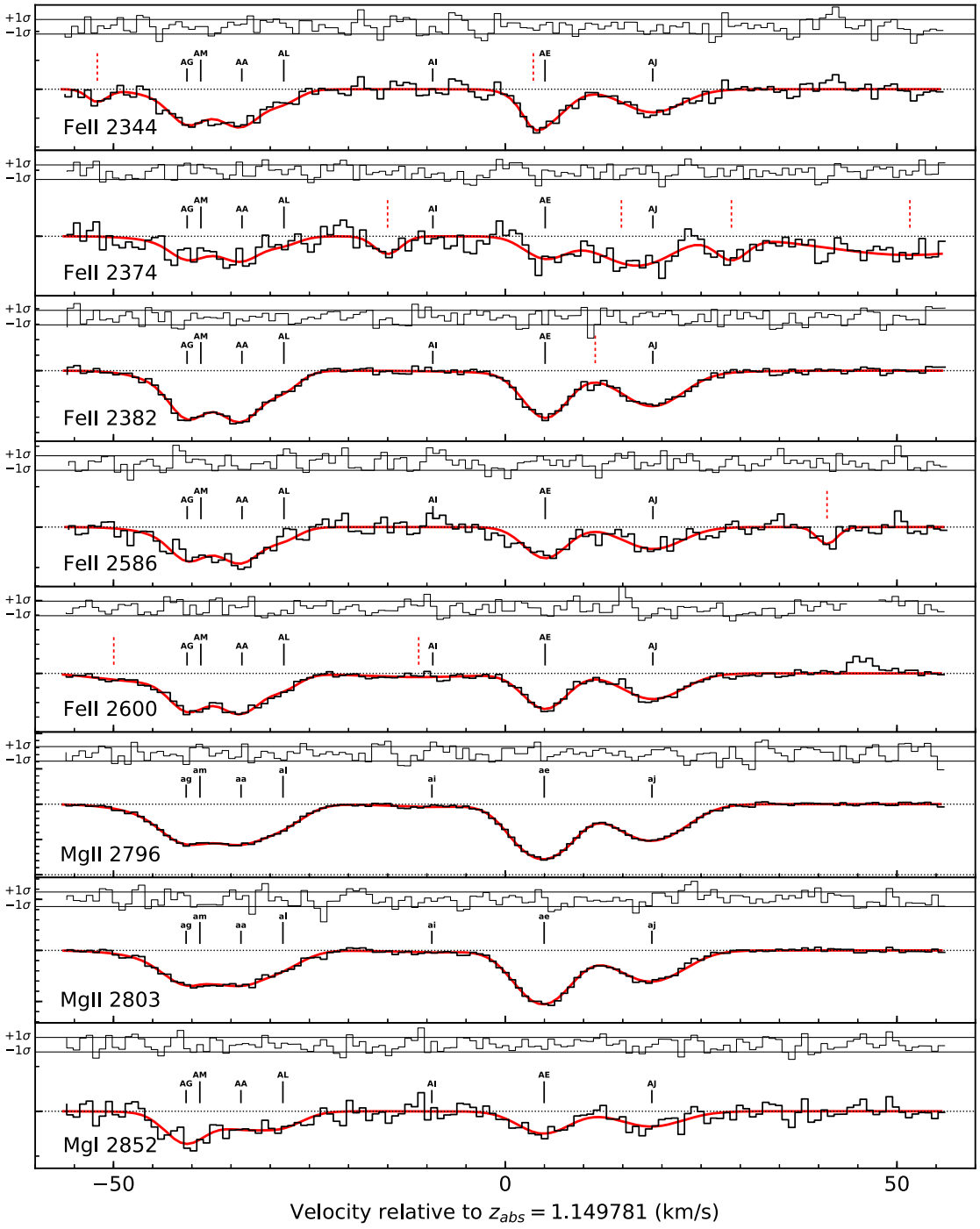

Figure B4. The same as in Fig. B1, except for LFC-calibrated spectral region IV.

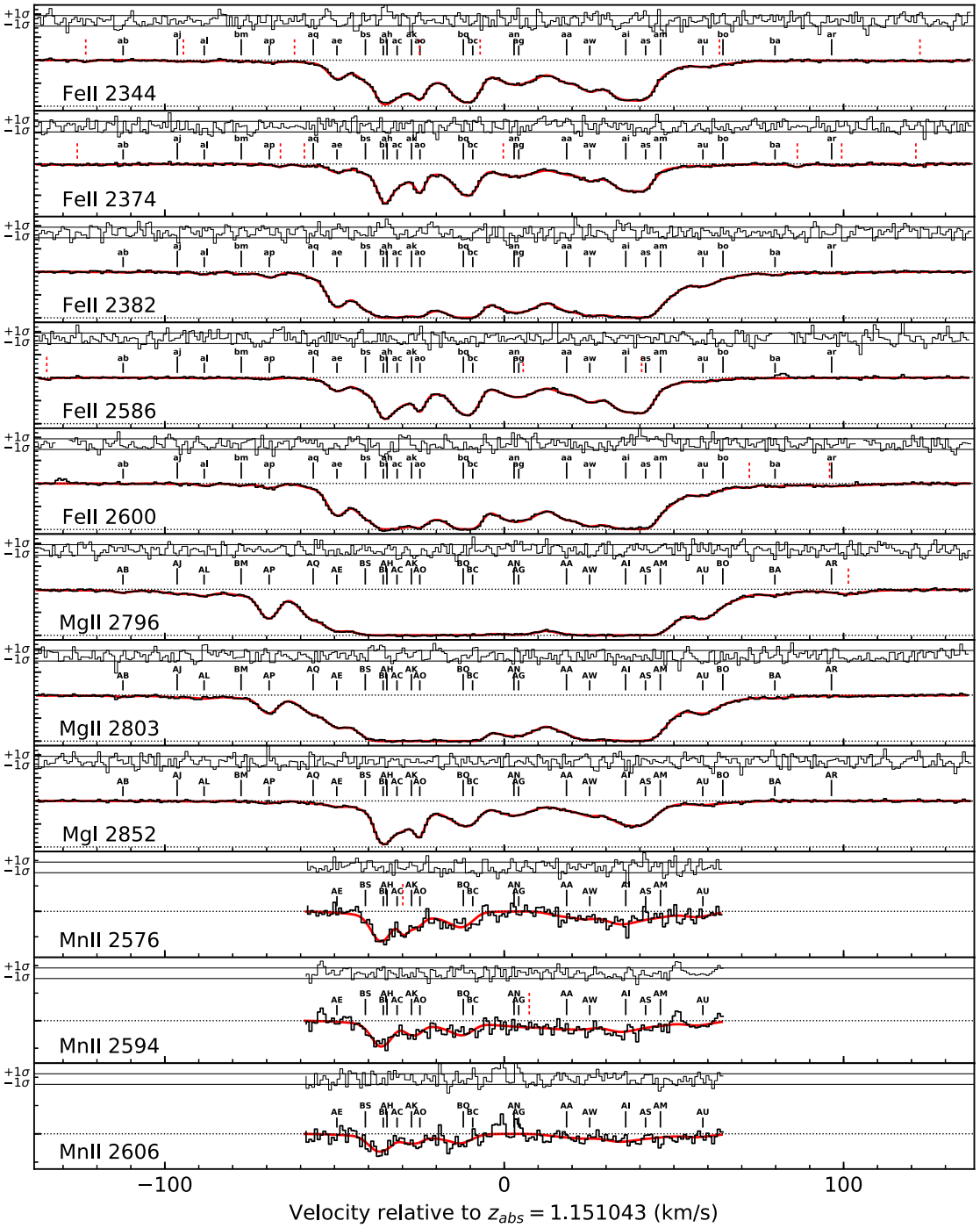

Figure B5. The same as in Fig. B1, except for LFC-calibrated spectral region V.

APPENDIX C: THAR-CALIBRATED MODELS

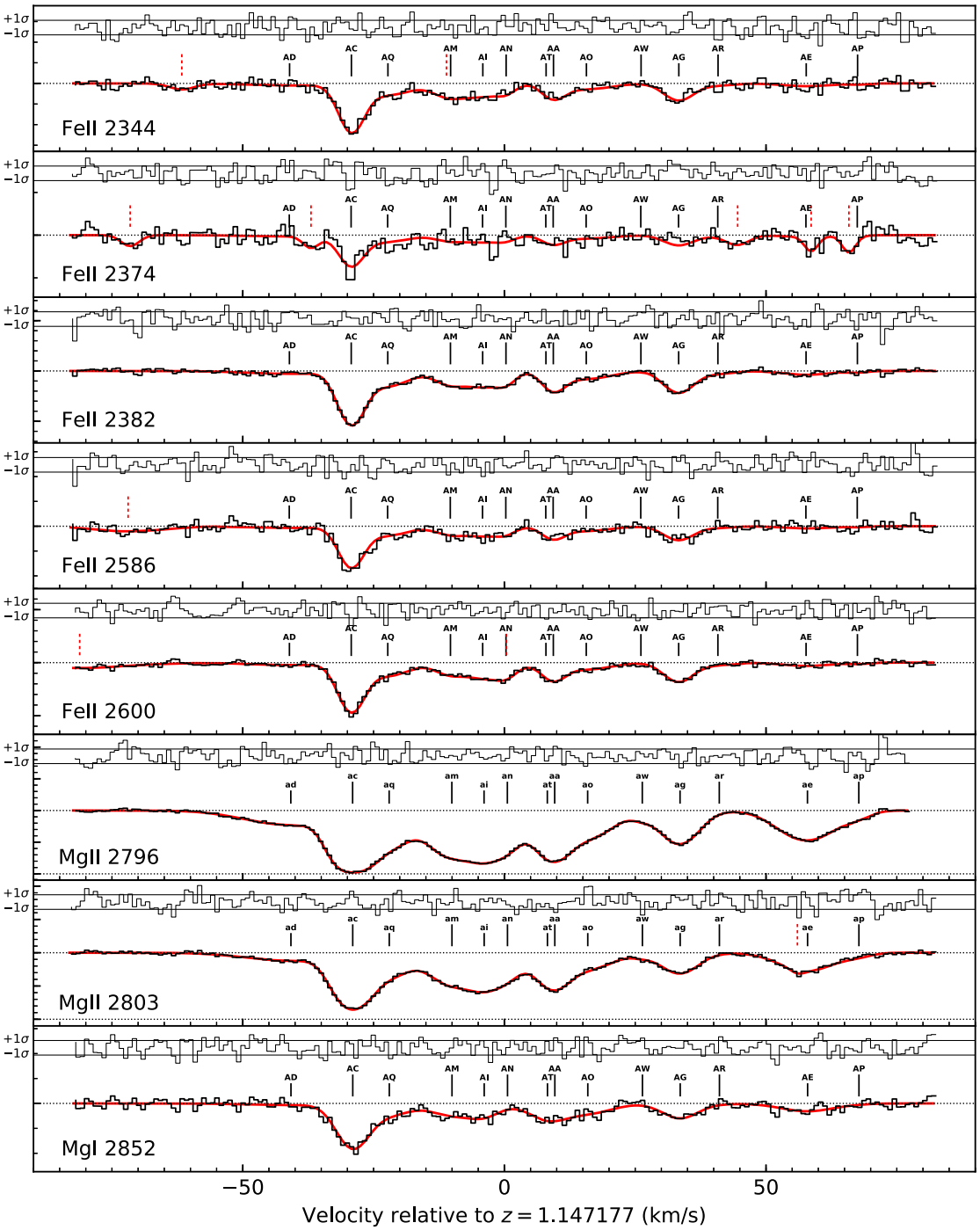

Figure C1. The same as in Fig. B1, except for ThAr-calibrated spectral region I.

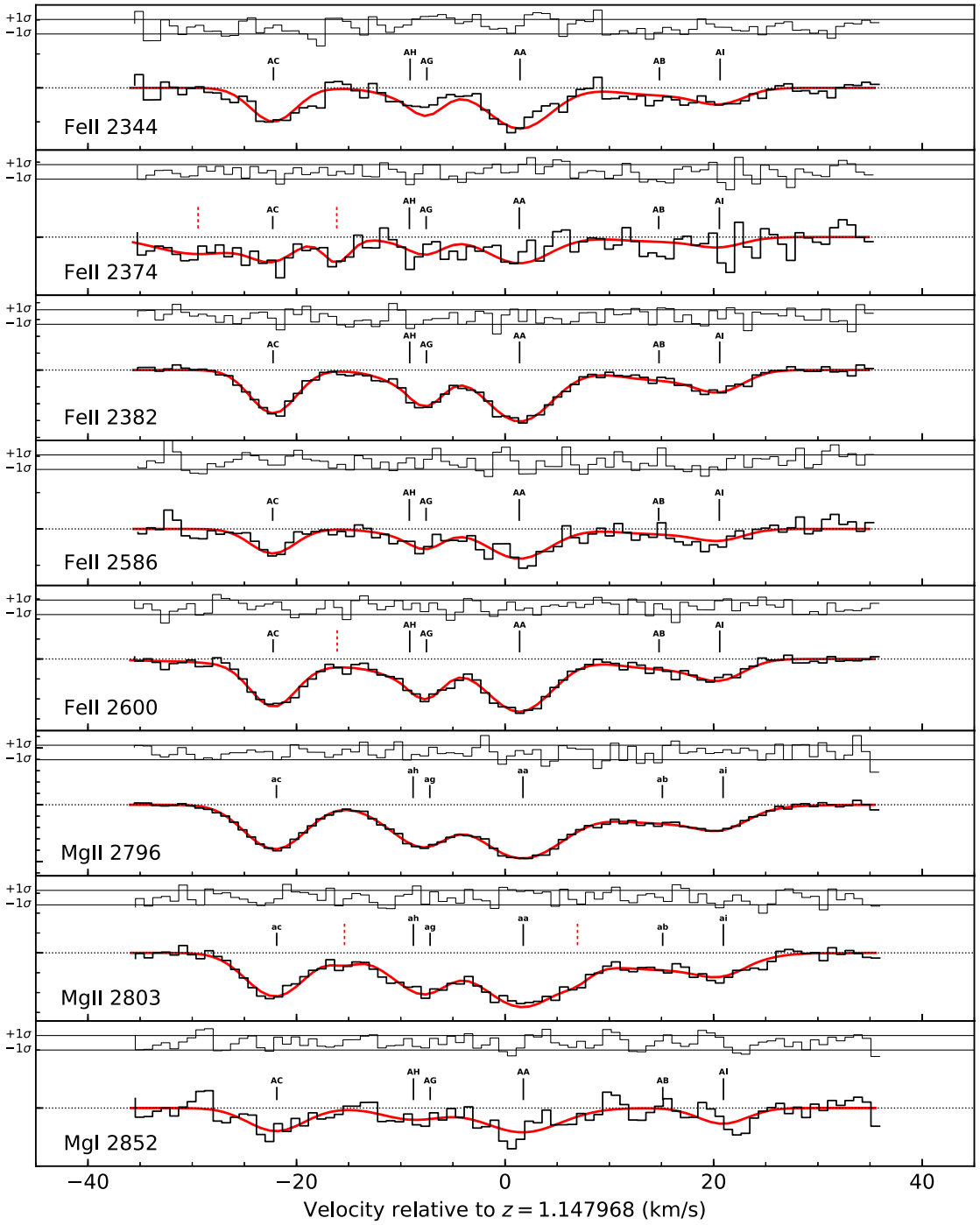

Figure C2. The same as in Fig. B1, except for ThAr-calibrated spectral region II.

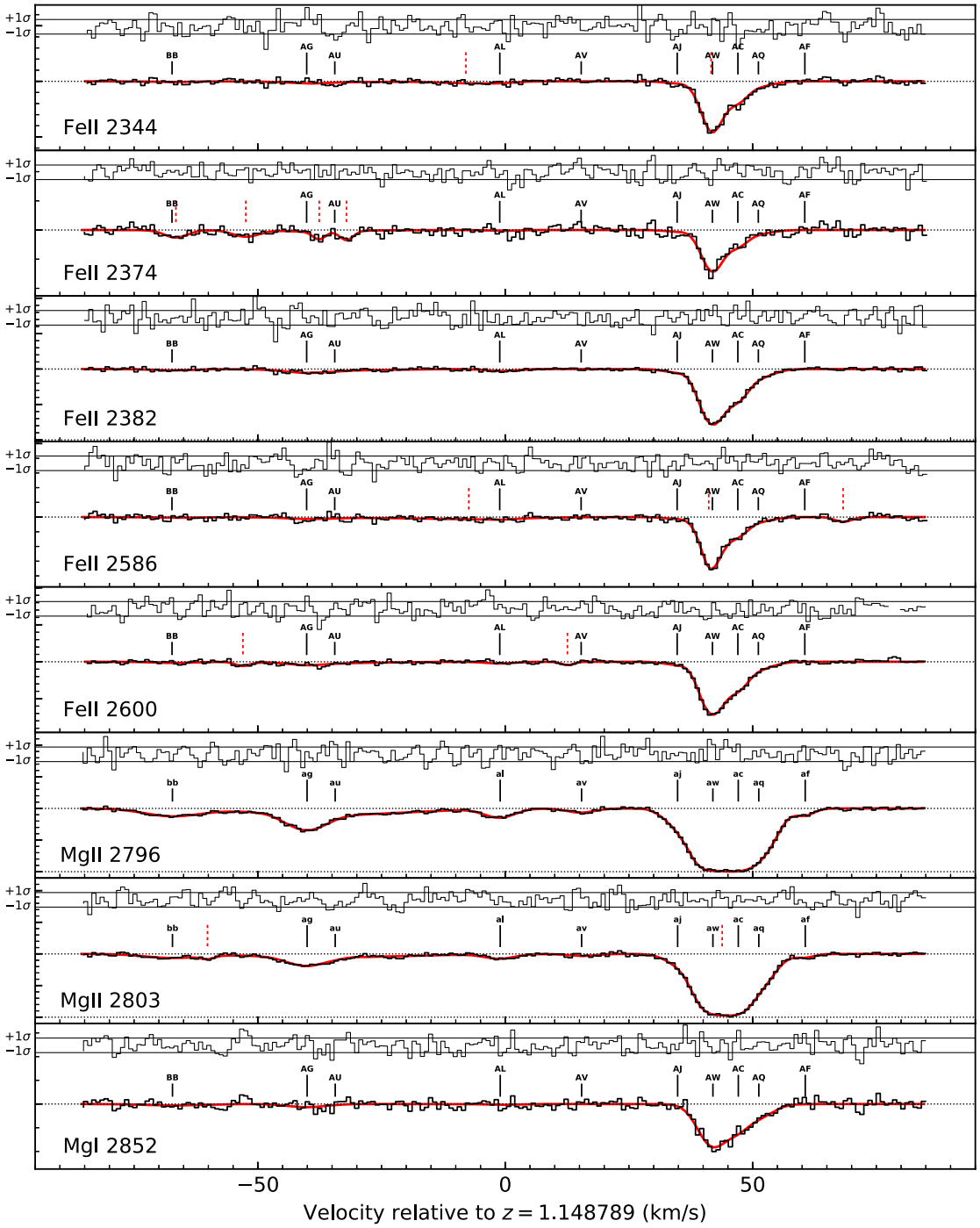

Figure C3. The same as in Fig. B1, except for ThAr-calibrated spectral region III.

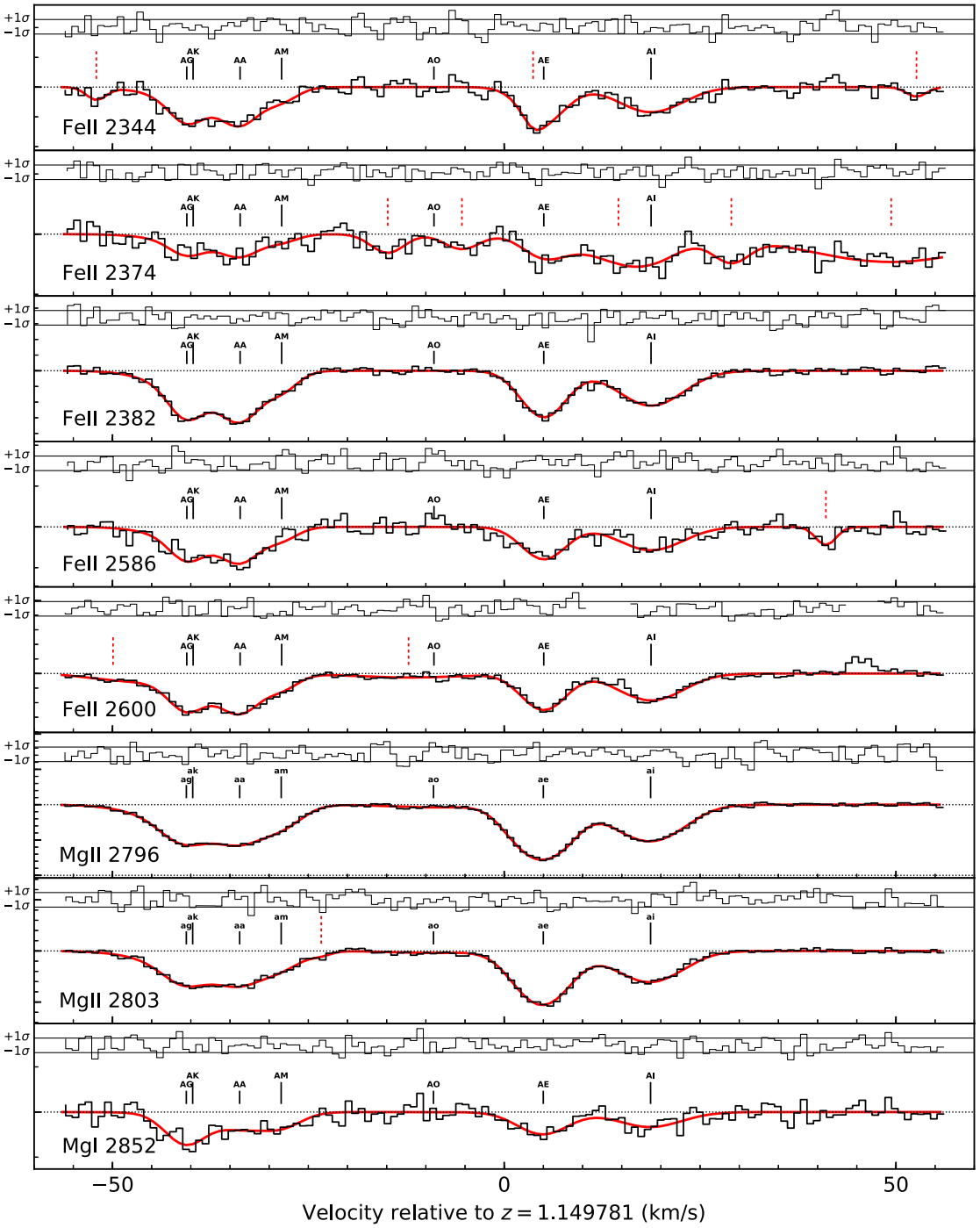

Figure C4. The same as in Fig. B1, except for ThAr-calibrated spectral region IV.

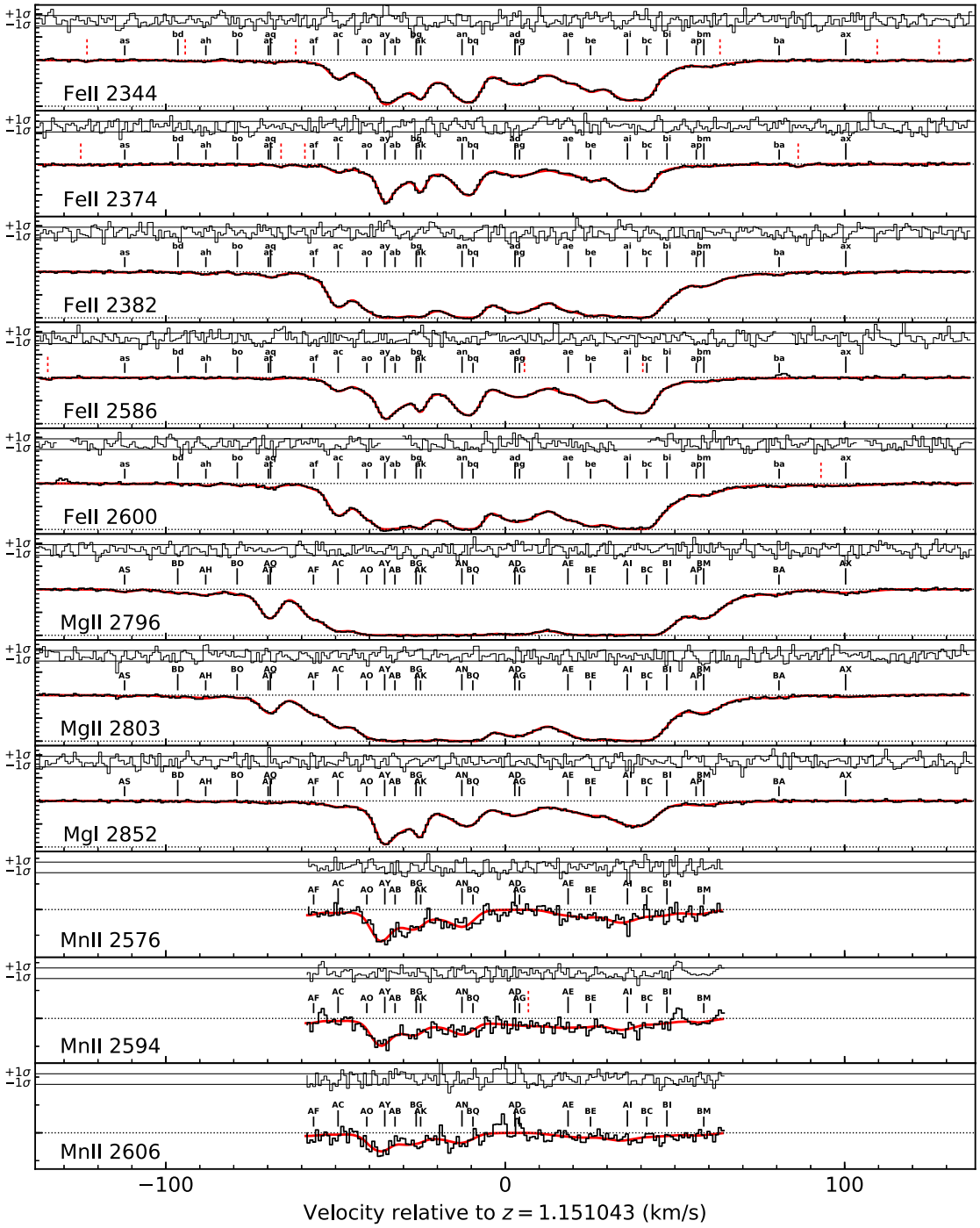

Figure C5. The same as in Fig. B1, except for ThAr-calibrated spectral region V.

This paper has been typeset from a TEX/LATEX file prepared by the author.